Geophys. J. Int. (2005) **161,** 81–101 doi: 10.1111/j.1365-246X.2005.02546.x

Time-domain, spherical harmonic-finite element approach to transient three-dimensional geomagnetic induction in a spherical heterogeneous Earth

Jakub Velímský* and Zdeněk Martinec†

Charles University in Prague, Czech Republic

Accepted 2004 December 2. Received 2004 August 10; in original form 2003 July 22

SUMMARY

We introduce a time-domain method to solve the problem of geomagnetic induction in a heterogeneous Earth excited by variations of the ionospheric and magnetospheric currents with arbitrary spatiotemporal characteristics. The problem is formulated in the integral sense. The Galerkin discretization is based on the vector spherical harmonic functions and piecewise linear finite elements in the angular and radial directions, respectively. A semi-implicit time integration scheme is employed. The method is validated against semi-analytical (SA) solutions for conductivity models consisting of multiple eccentrically nested homogeneous spheres.

Key words: electromagnetic induction, lateral conductivity variations, numerical modelling, spherical harmonics.

1 INTRODUCTION

The response of the conductive Earth's mantle to long-periodic variations of the ionospheric and magnetospheric currents represents the most effective way to determine the mantle conductivity. It has been intensively studied for a long time. The first inversions of the geomagnetic variations measured at the surface assumed a spherically symmetric distribution of conductivity in the Earth's mantle (e.g. Banks 1969). Results obtained by mantle convection modelling and by the three-dimensional (3-D) seismic tomography suggest that the lateral variations of temperature in the mantle are of orders of 10^2–10^3 K on the scales of 10^2–10^3 km (Duffy & Hemley 1995). These results and the laboratory measurements of conductivity under mantle pressure and temperature conditions (e.g. Xu *et al.* 1998) yield that the lateral conductivity variations of orders of magnitude can be expected in the mantle. Local one-dimensional (1-D) interpretations of carefully processed data strongly support this idea. Schultz & Larsen (1987) demonstrated that no single 1-D conductivity model is compatible with geomagnetic responses observed at geographically distributed observatories. The existence of lateral conductivity variations in the upper and middle mantle has been confirmed in other local 1-D and regional studies (see Tarits 1994, and references therein).

These results represented a strong motivation for the recent development of efficient forward solvers of the electromagnetic (EM) induction problem in a radially and laterally inhomogeneous Earth's mantle. Following the traditional frequency-domain approach, Fainberg *et al.* (1990) assumed a thin heterogeneous conductive sheet representing the high contrast between conducting oceans and resistive continents with underlying radially stratified medium. The problem was formulated as an integral equation for surface currents in the sheet and solved by means of an iterative–dissipative method. The method was later generalized for an arbitrary position of the heterogeneous thin sheet in the spherically symmetric Earth (Kuvshinov & Pankratov 1994). Zhang & Schultz (1992) developed a perturbation method for a radially symmetric conductivity model superposed by small lateral heterogeneities. Everett & Schultz (1996) and Yoshimura & Oshiman (2002) applied different finite element methods to the EM induction problem formulated in terms of EM potentials. A spectral-finite element (SFE) approach was introduced by Martinec (1999) and a staggered-grid finite difference method was implemented by Uyeshima & Schultz (2000).

The problem of EM induction in the mantle is traditionally approached in the frequency domain. The equation of EM induction is solved with the assumption of harmonic signals at discrete frequencies usually from the range of 10^{-2}–10^{0} cycle d^{-1}, covering the spectrum that corresponds to solar quiet (Sq) and disturbed (Dst) geomagnetic variations. However, the transient signals, such as magnetic storms, are sources of strong induction effects in the mantle as a result of abrupt changes of the system of external inducing electrical currents in the

*Also at: Department of Geology and Geophysics, Texas A&M University, College Station, TX 77843-3115, USA. E-mail: jakub.velimsky@mff.cuni.cz
†Also at: GeoForschungsZentrum Potsdam, Germany.

ionosphere and magnetosphere. It is inconvenient to study the response of the Earth to transient signals in the frequency domain because they have a broad spectrum.

One of the main obstacles in the inversion of the ground based long-periodic data to reveal a 3-D conductivity structure is the uneven spatial distribution of the geomagnetic observatories, especially the poor coverage of the oceanic areas. On the other hand, the satellite magnetometer data such as those obtained from the MAGSAT, Ørsted and CHAMP spacecrafts have excellent spatial coverage and offer an unprecedented opportunity to improve our knowledge of electrical conductivity in the Earth's mantle. The complicated spatiotemporal distribution of satellite data also favours a time-domain approach.

The time-domain approach to the EM induction problem was recently applied by Hamano (2002). The problem was formulated in terms of poloidal and toroidal functions. Spherical harmonic expansion and finite differences were used in the angular and radial parametrization, respectively. The Crank–Nicolson scheme was employed for the time integration.

In this paper, we present an alternative time-domain approach based on the spherical harmonic-finite element parametrization (Martinec 1999). We employ an effective semi-implicit time integration scheme. The terms containing the radial part of the conductivity are treated implicitly in time while the coupling terms resulting from the lateral conductivity variations are computed explicitly making use of the solution from the previous time step. The method is validated against fully 3-D semi-analytical (SA) solutions for conductivity models consisting of eccentrically nested homogeneous spheres (Martinec 1998).

2 FORMULATION OF THE INITIAL-VALUE PROBLEM

2.1 Classical formulation

Let us start with notation and basic assumptions. By $\mathbf{r}$ we denote the position vector, which is further expressed by spherical coordinates $\mathbf{r} = (r, \Omega) = (r, \vartheta, \varphi)$. We approximate the Earth by a sphere G with surface ∂G of radius a. We assume that the sphere G has constant magnetic permeability μ_0 and positive, finite, continuous 3-D varying electrical conductivity $\sigma(\mathbf{r}) \in L^+_\infty(G) \cap C^1(G)$ (see Appendix B for a summary of used functional spaces). It is also useful to introduce the electrical resistivity $\rho(\mathbf{r}) = 1/\sigma(\mathbf{r})$, $\rho(\mathbf{r}) \in L^+_\infty(G) \cap C^1(G)$. The magnetic field in G is induced by time-varying electrical currents $\mathbf{j}^{(e)}$ in the ionosphere and the magnetosphere, which are separated from the Earth by a perfectly insulating spherical atmosphere A. The model configuration is sketched in Fig. 1. The characteristic timescales of the external current variations range from several hours to hundreds of days, so the quasi-static approximation of Maxwell's equations is applicable.

Under these assumptions, the equation of EM induction can be derived directly from Maxwell's equations (Parkinson & Hutton 1989):

$$\mu_0 \frac{\partial \mathbf{B}}{\partial t} + \mathrm{curl}(\rho \,\mathrm{curl}\, \mathbf{B}) = 0 \quad \text{in } G, \tag{1}$$

where $\mathbf{B}(\mathbf{r}; t) \in C^2(G)^3 \times C^1(\langle 0, \infty))^3$ is the vector of magnetic induction. Eq. (1) is a parabolic differential equation. The initial value and the boundary value conditions of $\mathbf{B}$ must be specified to complete the formulation. The initial value ${}^0\mathbf{B}$ at time $t = 0$ is specified by a function from $C^2(G)^3$ that satisfies the divergence-free condition

$$\mathrm{div}\, {}^0\mathbf{B} = 0 \quad \text{in } G. \tag{2}$$

Applying the divergence operator on eq. (1) yields

$$\frac{\partial (\mathrm{div}\, \mathbf{B})}{\partial t} = 0 \quad \text{in } G. \tag{3}$$

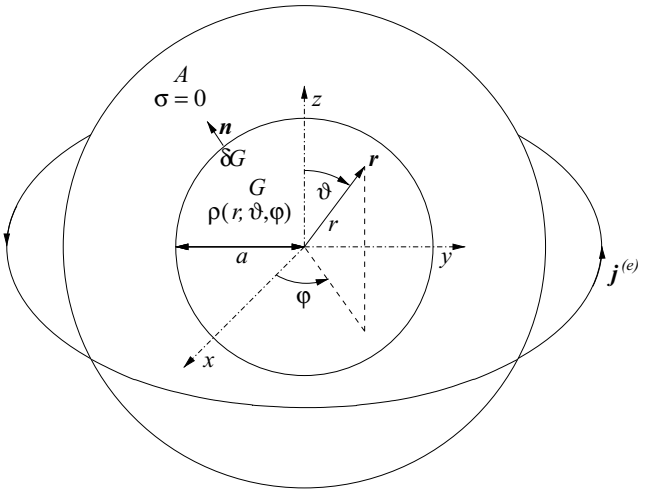

Figure 1. A schematic figure of model configuration. Heterogeneous conductive sphere G of radius a with surface ∂G is surrounded by an insulating spherical layer A. Above A, a system of primary inducing electrical currents $\mathbf{j}^{(e)}$ is prescribed.

Eq. (3) and the choice of ${}^0\mathbf{B}$ in accordance with eq. (2) assure that div $\mathbf{B} = 0$ at any time $t > 0$, i.e. the divergence-free condition on $\mathbf{B}$ is implicitly satisfied by the equation of EM induction (1).

The general form of the boundary conditions imposed on the magnetic field by Maxwell's equations on any material interface is,

$$[\mathbf{n} \cdot \mathbf{B}]^+_- = 0, \tag{4}$$

$$[\mathbf{n} \times \mathbf{H}]^+_- = \mathbf{j}_S, \tag{5}$$

where $\mathbf{H}$, $\mathbf{j}_S$ and $\mathbf{n}$ are the magnetic intensity vector, the density of free surface currents and the unit normal vector on the interface, respectively. Because of the assumption of constant magnetic permeability μ_0 in the material relation

$$\mathbf{B} = \mu_0 \mathbf{H} \tag{6}$$

and because no free surface currents are generated on the surfaces of finitely conducting, or insulating bodies, the boundary conditions imposed on $\mathbf{B}$ on ∂G reduce to

$$[\mathbf{B}]^+_- = 0. \tag{7}$$

The magnetic induction vector $\mathbf{B}$ changes continuously across the spherical surface ∂G.

The magnetic induction in the insulating atmosphere A is a divergence-free and irrotational field, and can be represented at any time $t \geq 0$ by a gradient of scalar magnetic potential $U(\mathbf{r}; t)$:

$$\mathbf{B}(\mathbf{r}; t) = -\mathrm{grad} U(\mathbf{r}; t) \quad \text{in } A, \tag{8}$$

where U satisfies the Laplace equation,

$$\nabla^2 U(\mathbf{r}; t) = 0 \quad \text{in } A. \tag{9}$$

Expanding the magnetic potential into a series of spherical harmonics $Y_{jm}(\Omega)$ (Varshalovich *et al.* 1989, p. 130) allows us to write the analytical solution of eq. (9) as a sum of two parts,

$$U = U^{(e)} + U^{(i)}. \tag{10}$$

The external part,

$$U^{(e)}(\mathbf{r}; t) = a \sum_{j=1}^{\infty} \sum_{m=-j}^{j} G^{(e)}_{jm}(t) \left(\frac{r}{a}\right)^j Y_{jm}(\Omega), \tag{11}$$

represents the magnetic field induced by ionospheric and magnetospheric currents $\mathbf{j}^{(e)}$ above the atmospheric layer A. The internal part,

$$U^{(i)}(\mathbf{r}; t) = a \sum_{j=1}^{\infty} \sum_{m=-j}^{j} G^{(i)}_{jm}(t) \left(\frac{a}{r}\right)^{j+1} Y_{jm}(\Omega), \tag{12}$$

represents the magnetic field of induced currents inside the sphere G (e.g. Langel 1987). Substituting from eqs (10), (11) and (12) into eq. (8), and taking into account the formula for gradient of spherical harmonic functions (A15), yields

$$\mathbf{B}(\mathbf{r}; t) = \mathbf{B}^{(e)}(\mathbf{r}; t) + \mathbf{B}^{(i)}(\mathbf{r}; t) \quad \text{in } A, \tag{13}$$

where

$$\mathbf{B}^{(e)}(\mathbf{r}; t) = -\sum_{jm} G^{(e)}_{jm}(t) \left(\frac{r}{a}\right)^{j-1} \left[j \mathbf{S}^{(-1)}_{jm}(\Omega) + \mathbf{S}^{(1)}_{jm}(\Omega)\right], \tag{14}$$

$$\mathbf{B}^{(i)}(\mathbf{r}; t) = \sum_{jm} G^{(i)}_{jm}(t) \left(\frac{a}{r}\right)^{j+2} \left[(j+1) \mathbf{S}^{(-1)}_{jm}(\Omega) - \mathbf{S}^{(1)}_{jm}(\Omega)\right]. \tag{15}$$

The vector spherical harmonic functions $\mathbf{S}^{(\lambda)}_{jm}(\Omega)$, $\lambda = -1, 0, 1$, are introduced in Appendix A. The limits in the sums over j and m remain the same as in eq. (11) and will be omitted from now on. The downward, northward and eastward components of magnetic induction in the atmosphere can be derived from the definitions (A4)–(A6):

$$\begin{aligned} Z(\mathbf{r}; t) &= -\mathbf{e}_r \cdot \mathbf{B}(\mathbf{r}; t) \\ &= \sum_{jm} \left[j G^{(e)}_{jm}(t) \left(\frac{r}{a}\right)^{j-1} - (j+1) G^{(i)}_{jm}(t) \left(\frac{a}{r}\right)^{j+2} \right] Y_{jm}(\Omega), \end{aligned} \tag{16}$$

$$\begin{aligned} X(\mathbf{r}; t) &= -\mathbf{e}_\vartheta \cdot \mathbf{B}(\mathbf{r}; t) \\ &= \sum_{jm} \left[G^{(e)}_{jm}(t) \left(\frac{r}{a}\right)^{j-1} + G^{(i)}_{jm}(t) \left(\frac{a}{r}\right)^{j+2} \right] \frac{\partial Y_{jm}}{\partial \vartheta}(\Omega), \end{aligned} \tag{17}$$

$$Y(\mathbf{r};t) = \mathbf{e}_\varphi \cdot \mathbf{B}(\mathbf{r};t)$$
$$= \frac{-1}{\sin\vartheta}\sum_{jm}\left[G^{(e)}_{jm}(t)\left(\frac{r}{a}\right)^{j-1} + G^{(i)}_{jm}(t)\left(\frac{a}{r}\right)^{j+2}\right]\frac{\partial Y_{jm}}{\partial\varphi}(\Omega). \tag{18}$$

The unit vectors corresponding to the radial coordinate r, colatitude ϑ and longitude φ, are denoted by $\mathbf{e}_r$, $\mathbf{e}_\vartheta$, and $\mathbf{e}_\varphi$. Note that $\mathbf{e}_r = \mathbf{n}$ on ∂G. Spherical harmonic coefficients of the external and internal potential, $G^{(e)}_{jm}(t)$ and $G^{(i)}_{jm}(t)$, can be determined from components X, Y, Z measured at ground based observatories or at a low-altitude satellite orbit. This problem, although important in 3-D inversions for the conductivity structure, is not discussed in this work.

To express the boundary condition at the surface of the Earth, we expand the magnetic induction vector inside the sphere G into a series of vector spherical harmonics,

$$\mathbf{B}(r,\Omega;t) = \sum_{j=1}^{\infty}\sum_{m=-j}^{j}\sum_{\lambda=-1}^{1} B^{(\lambda)}_{jm}(r;t)\mathbf{S}^{(\lambda)}_{jm}(\Omega), \tag{19}$$

where $B^{(\lambda)}_{jm}(r;t)$ are complex functions of radius and time. Because we use complex parametrization to represent real functions, the property (A11) of the spherical harmonics yields

$$B^{(\lambda)}_{j-m}(r;t) = (-1)^m\overline{B}^{(\lambda)}_{jm}(r;t). \tag{20}$$

Assuming the continuity of $\mathbf{B}$ for $r = a$ in eqs (13)–(15) and (19) leads to

$$B^{(0)}_{jm}(a;t) = 0, \tag{21}$$

$$B^{(-1)}_{jm}(a;t) = -\left[jG^{(e)}_{jm}(t) - (j+1)G^{(i)}_{jm}(t)\right], \tag{22}$$

$$B^{(1)}_{jm}(a;t) = -\left[G^{(e)}_{jm}(t) + G^{(i)}_{jm}(t)\right]. \tag{23}$$

The spherical harmonic coefficients appropriate to the toroidal part, $B^{(0)}_{jm}$, vanish at the boundary ∂G, the external and internal parts of the magnetic potential are present in the vertical spheroidal components $B^{(-1)}_{jm}$ and in the horizontal spheroidal components $B^{(1)}_{jm}$. By eliminating $G^{(i)}_{jm}(t)$ from (22) and (23), we can reduce the boundary conditions to

$$B^{(0)}_{jm}(a;t) = 0, \tag{24}$$

$$B^{(-1)}_{jm}(a;t) + (j+1)B^{(1)}_{jm}(a;t) = -(2j+1)G^{(e)}_{jm}(t). \tag{25}$$

The boundary conditions (24)–(25) are connected to the spherical harmonic expansion of $\mathbf{B}$ and cannot be expressed as simple Dirichlet or Neumann boundary conditions imposed on $\mathbf{B}$. Therefore, they are difficult to implement in other numerical schemes, such as 3-D finite elements, or 3-D finite differences. In such cases, the Laplace eq. (9) is solved numerically and boundary condition on potential U is prescribed on the outer surface of A (Everett & Schultz 1996; Uyeshima & Schultz 2000). However, using the orthogonality of the spherical harmonic functions (A8), it is possible to reformulate eqs (24)–(25) as a set of integral equations

$$\int_\Omega \mathbf{B}(a,\Omega;t)\cdot\overline{\mathbf{S}}^{(0)}_{jm}(\Omega)\,\mathrm{d}\Omega = 0, \tag{26}$$

$$\int_\Omega \mathbf{B}(a,\Omega;t)\cdot\left[\overline{\mathbf{S}}^{(-1)}_{jm}(\Omega) + \frac{1}{j}\overline{\mathbf{S}}^{(1)}_{jm}(\Omega)\right]\mathrm{d}\Omega = -(2j+1)G^{(e)}_{jm}(t), \tag{27}$$

which hold for each $j \geq 1$ and m, such that $|m| \leq j$. Bar denotes complex conjugation.

Now we can finally summarize the formulation of the EM induction problem in the time domain in the classical sense:

Let $\mu_0 > 0$ and $\rho(\mathbf{r}) \in L^+_\infty(G) \cap C^1(G)$. Let the initial value ${}^0\mathbf{B}(\mathbf{r}) \in C^2(G)^3$ be a divergence − free function, $\mathrm{div}\,{}^0\mathbf{B} = 0$ in G. Let $U^{(e)}(r,\Omega;t)$ be the external part of magnetic potential in the atmosphere defined by eq. (11). Find such a function $\mathbf{B}(\mathbf{r};t) \in C^2(G)^3 \times C^1(\langle 0,\infty\rangle)^3$ that satisfies

$$\mu_0\frac{\partial\mathbf{B}}{\partial t} + \mathrm{curl}\,(\rho\ \mathrm{curl}\ \mathbf{B}) = 0 \quad \text{in } G, \tag{28}$$

$$\mathbf{B}(\mathbf{r};0) = {}^0\mathbf{B}(\mathbf{r}) \quad \text{in } G, \tag{29}$$

and $\forall j \geq 1,\ |m| \leq j$,

$$\int_\Omega \mathbf{B}(a,\Omega;t)\cdot\overline{\mathbf{S}}^{(0)}_{jm}(\Omega)\,\mathrm{d}\Omega = 0, \tag{30}$$

$$\int_\Omega \mathbf{B}(a,\Omega;t)\cdot\left[\overline{\mathbf{S}}^{(-1)}_{jm}(\Omega) + \frac{1}{j}\overline{\mathbf{S}}^{(1)}_{jm}(\Omega)\right]\mathrm{d}\Omega = -(2j+1)G^{(e)}_{jm}(t). \tag{31}$$

It is also possible to extend the classical formulation (28)–(31) to the case of discontinuous resistivity in G. Let us assume internal surfaces Γ_i, where resistivity $\rho(\mathbf{r})$ changes discontinuously, separating the sphere G into subdomains G_i, where $\rho(\mathbf{r})$ is continuous. Then the eq. (28) holds in each subdomain G_i and continuity of $\mathbf{B}$ (eq. 7) is imposed on the internal interfaces Γ_i.

2.2 Integral (weak) formulation

To reformulate the problem of EM induction in a heterogeneous sphere in the integral sense, we introduce the solution spaces H_{curl}, $H_{\text{curl},0}$ (Křížek & Neittaanmäki 1990, p. 142) and the L_2 scalar product $(\cdot, \cdot)$ (see Appendix B). Then we can pose the problem as follows.

Let $\mu_0 > 0$ and $\rho(\mathbf{r}) \in L^+_\infty(G)$. Let the initial value ${}^0\mathbf{B}(\mathbf{r}) \in H_{\text{curl}}$ be a divergence-free function, $\operatorname{div}{}^0\mathbf{B} = 0$ in G. Let $U^{(e)}(r, \Omega; t)$ be the external part of magnetic potential in the atmosphere defined by eq. (11). Find $\mathrm{B}(\mathrm{r};t) \in H_{\text{curl}} \times C^1(\langle 0, \infty)\rangle)^3$, such that

$$\mu_0 \left(\frac{\partial \mathbf{B}}{\partial t}, \delta\mathbf{B} \right) + a(\mathbf{B}, \delta\mathbf{B}) = 0 \quad \forall\, \delta\mathbf{B} \in H_{\text{curl},0}, \tag{32}$$

$$\mathbf{B}(\mathbf{r}; 0) = {}^0\mathbf{B}(\mathbf{r}) \quad \text{in } G, \tag{33}$$

and $\forall\, j \geq 1,\ |m| \leq j$,

$$\int_\Omega \mathbf{B}(a, \Omega; t) \cdot \overline{\mathbf{S}}^{(0)}_{jm}(\Omega)\, \mathrm{d}\Omega = 0, \tag{34}$$

$$\int_\Omega \mathbf{B}(a, \Omega; t) \cdot \left[\overline{\mathbf{S}}^{(-1)}_{jm}(\Omega) + \frac{1}{j} \overline{\mathbf{S}}^{(1)}_{jm}(\Omega) \right] \mathrm{d}\Omega = -(2j+1) G^{(e)}_{jm}(t). \tag{35}$$

The sesquilinear form $a(\cdot\,, \cdot)$ is defined as

$$a(\mathbf{B}, \delta\mathbf{B}) = \int_G \rho (\operatorname{curl}\mathbf{B}) \cdot (\operatorname{curl}\delta\mathbf{B})\, \mathrm{d}V. \tag{36}$$

Let us show that if there exists a weak solution of eqs (32)–(35), such that $\mathbf{B} \in C^2(G)^3 \times C^1(\langle 0, \infty)\rangle)^3$, for $\rho \in C^1(G)$ and ${}^0\mathbf{B} \in C^2(G)^3$, it is also the classical solution of eqs (28)–(31). Because $C^2(G)^3 \subset H_{\text{curl}}$, we can take $\delta\mathbf{B} \in C^2(G)$, such that $\mathbf{e}_r \times \delta\mathbf{B} = 0$ on ∂G, and apply on eq. (32) Green's theorem,

$$\int_G \operatorname{curl}\,(h\, \operatorname{curl}\mathbf{f}) \cdot \mathbf{g}\, \mathrm{d}V = \int_G h\, (\operatorname{curl}\mathbf{f}) \cdot (\operatorname{curl}\mathbf{g})\, \mathrm{d}V - \int_{\partial G} h\, (\operatorname{curl}\mathbf{f}) \cdot (\mathbf{e}_r \times \mathbf{g})\, \mathrm{d}S, \tag{37}$$

valid for any $h \in C^1(G)$, $\mathbf{f}, \mathbf{g} \in C^2(G)^3$. The surface integral is cancelled because of the choice of $\delta\mathbf{B}$ and we are left with

$$\int_G \left[\mu_0 \frac{\partial \mathbf{B}}{\partial t} + \operatorname{curl}\,(\rho \operatorname{curl}\mathbf{B}) \right] \cdot \delta\mathbf{B}\, \mathrm{d}V = 0. \tag{38}$$

This can be satisfied for all $\delta\mathbf{B} \in C^2(G)$, $\mathbf{e}_r \times \delta\mathbf{B} = 0$ on ∂G, only if

$$\mu_0 \frac{\partial \mathbf{B}}{\partial t} + \operatorname{curl}(\rho \operatorname{curl}\mathbf{B}) = 0 \quad \text{in } G. \tag{39}$$

The integral formulation also implicitly satisfies the divergence-free constraint on $\mathbf{B}$. Let us introduce an auxiliary function $\xi \in D^0(G)$ and construct a particular test functions $\delta\mathbf{B} = \operatorname{grad}\xi$. Note that $\delta\mathbf{B} \in H_{\text{curl},0}$ because $\operatorname{grad}\xi \in L_2(G)^3$, $\operatorname{curl}\operatorname{grad}\xi = 0$ and $\mathbf{e}_r \times \operatorname{grad}\xi = 0$ on ∂G. Then eq. (32) yields

$$\int_G \frac{\partial \mathbf{B}}{\partial t} \cdot \operatorname{grad}\xi\, \mathrm{d}V = 0 \quad \forall \xi \in D^0(G). \tag{40}$$

Because $H_{\text{curl}} \subset L_2(G)^3$ and $D^0(G) \subset L_2(G)$, we can use another Green's theorem that holds for any square integrable scalar h and vector $\mathbf{f}$,

$$\int_G \mathbf{f} \cdot \operatorname{grad} h\, \mathrm{d}V = -\int_G (\operatorname{div}\mathbf{f})\, h\, \mathrm{d}V + \int_{\partial G} (\mathbf{e}_r \cdot \mathbf{f})\, h\, dS. \tag{41}$$

The surface integral is zero because $\xi = 0$ on ∂G, and the time and space derivatives are interchangeable, therefore we can write

$$\int_G \frac{\partial(\operatorname{div}\mathbf{B})}{\partial t} \xi\, \mathrm{d}V = 0 \quad \forall \xi \in D^0(G). \tag{42}$$

This can be satisfied only with

$$\frac{\partial(\operatorname{div}\mathbf{B})}{\partial t} = 0 \quad \text{in } G. \tag{43}$$

However, numerical errors can introduce spurious magnetic monopoles during the time integration. This can be avoided either by adding the divergence-free constraint to eq. (32) in the form of the Lagrange multipliers (Martinec 1999), or by a projection to the divergence-free

solution (Uyeshima & Schultz 2000). Although a modified formulation of the presented method that uses the former approach to assure solenoidality of **B** was also developed, we have not observed any recognizable deviations from the divergence-free solution while testing the code for a wide selection of resistivity models and external source currents, and the constraint was dropped from the algorithm in favour of increased speed and lower memory requirements of the numerical method.

2.3 Time integration scheme

Implicit time integration schemes for solving parabolic differential equations are generally preferred to explicit ones (Press *et al.* 1992, p. 838). However, with fully 3-D resistivity distribution and as a result of the traditional spherical harmonic parametrization used in the angular coordinates, the form $a(\cdot, \cdot)$ leads to a very large matrix. Martinec (1999) proposed a method for a fast iterative solution of such a system, but it would still require to compute many iterations at each level of the time discretization. We present a different, semi-implicit approach, based on splitting of the form $a(\cdot, \cdot)$ into two parts.

Let us express the resistivity as a sum of two components:

$$\rho(r, \Omega) = \rho_0(r) + \rho_1(r, \Omega), \tag{44}$$

where $\rho_0(r) \in L^+_\infty(G)$ is a spherically symmetric, finite and positive resistivity model, and $\rho_1(r, \Omega)$ represents the deviations (not necessarily small) of the actual resistivity ρ from the spherically symmetric model. We experienced the best numerical results by prescribing ρ_0 as a maximum of ρ over angular coordinates:

$$\rho_0(r) = \max_\Omega \rho(r, \Omega). \tag{45}$$

Now we can split the sesquilinear form (36) into two parts corresponding to ρ_0 and ρ_1, respectively:

$$a(\mathbf{B}, \delta\mathbf{B}) = a_0(\mathbf{B}, \delta\mathbf{B}) + a_1(\mathbf{B}, \delta\mathbf{B}), \tag{46}$$

where

$$a_0(\mathbf{B}, \delta\mathbf{B}) = \int_G \rho_0(\operatorname{curl}\mathbf{B}) \cdot (\operatorname{curl}\delta\mathbf{B})\, \mathrm{d}V, \tag{47}$$

$$a_1(\mathbf{B}, \delta\mathbf{B}) = \int_G \rho_1(\operatorname{curl}\mathbf{B}) \cdot (\operatorname{curl}\delta\mathbf{B})\, \mathrm{d}V. \tag{48}$$

As we will show later, the form $a_0(\cdot, \cdot)$ is represented by a banded matrix with nine non-zero diagonals. Therefore, it is easy to treat it implicitly in the time integration scheme, while more complex form $a_1(\cdot, \cdot)$ is considered on the right-hand side of eq. (32) and is evaluated using the solution **B** from the previous time step.

Approximating the time derivative by the difference between the values of magnetic field at two following time steps,

$$\frac{\partial\mathbf{B}}{\partial t} \approx \frac{{}^{i+1}\mathbf{B} - {}^{i}\mathbf{B}}{\Delta t}, \tag{49}$$

where ${}^{i}\mathbf{B} = \mathbf{B}(\mathbf{r}; t_i) \in H_{\mathrm{curl}}$ and the time step $\Delta t = t_{i+1} - t_i$ is considered constant, we can formulate the time integration scheme as a sequence of elliptic problems with integral boundary conditions.

Find ${}^{i+1}\mathbf{B} \in H_{\mathrm{curl}}\ \forall\, i = 0, 1, \ldots,$ such that

$$\frac{\mu_0}{\Delta t}({}^{i+1}\mathbf{B}, \delta\mathbf{B}) + a_0({}^{i+1}\mathbf{B}, \delta\mathbf{B}) = \frac{\mu_0}{\Delta t}({}^{i}\mathbf{B}, \delta\mathbf{B}) - a_1({}^{i}\mathbf{B}, \delta\mathbf{B}) \quad \forall\delta\mathbf{B} \in H_{\mathrm{curl},0}, \tag{50}$$

and $\forall\, j \geq 1,\ |m| \leq j,$

$$\int_\Omega {}^{i+1}\mathbf{B}(a, \Omega) \cdot \overline{\mathbf{S}}^{(0)}_{jm}(\Omega)\, \mathrm{d}\Omega = 0, \tag{51}$$

$$\int_\Omega {}^{i+1}\mathbf{B}(a, \Omega) \cdot \left[\overline{\mathbf{S}}^{(-1)}_{jm}(\Omega) + \frac{1}{j}\overline{\mathbf{S}}^{(1)}_{jm}(\Omega)\right] \mathrm{d}\Omega = -(2j+1)G^{(e)}_{jm}(t_{i+1}). \tag{52}$$

The initial value ${}^{0}\mathbf{B}$ from eq. (33) is used on the right-hand side of eq. (50) for $i = 0$. Note that the solution ${}^{i+1}\mathbf{B}$ and the test functions $\delta\mathbf{B}$ are from different functional spaces H_{curl} and $H_{\mathrm{curl},0}$, respectively.

2.4 Spherical harmonic-finite element parametrization

The expansion of the magnetic induction **B** into a series of vector spherical harmonics has been introduced by eq. (19). To complete the spatial discretization of the problem (50)–(52), we need to define a parametrization over the radial coordinate. We use piecewise linear finite elements

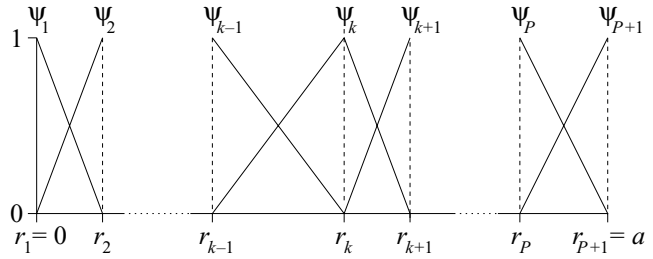

Figure 2. One-dimensional (1-D) piecewise linear finite element functions.

for this purpose. Let us divide the interval $\langle 0, a\rangle$ into P subintervals $\mathcal{I}_k = \langle r_k, r_{k+1}\rangle$, where $0 = r_1 < r_2 < \ldots < r_P < r_{P+1} = a$. In each interval $\mathcal{I}_k$, there are only two non-zero finite element functions, namely

$$\psi_k(r) = \frac{r_{k+1} - r}{h_k}, \qquad \psi_{k+1}(r) = \frac{r - r_k}{h_k}, \tag{53}$$

where $h_k = r_{k+1} - r_k$ is the length of the interval $\mathcal{I}_k$ (see Fig. 2).

Now we are ready to introduce the discrete approximation of the functional space H_{curl}:

$$H^h_{\mathrm{curl}} = \left\{ \mathbf{B} \,\middle|\, \mathbf{B} = \sum_{j=1}^{j_{\max}} \sum_{m=-j}^{j} \sum_{k=1}^{P+1} \sum_{\lambda=-1}^{1} B^{(\lambda)}_{jm,k} \psi_k \mathbf{S}^{(\lambda)}_{jm} \right\}. \tag{54}$$

The spherical harmonic expansion is truncated at finite degree $j_{\max}$. Note that the spherical harmonic coefficients $B^{(\lambda)}_{jm,k}$ must satisfy the discrete form of eq. (20),

$$B^{(\lambda)}_{j-m,k} = (-1)^m \overline{B}^{(\lambda)}_{jm,k}, \tag{55}$$

because $\mathbf{B}$ is real. By excluding the basis functions $\psi_{P+1}\mathbf{S}^{(0)}_{jm}$ and $\psi_{P+1}\mathbf{S}^{(1)}_{jm}$, which have non-zero horizontal components at the surface, we get an approximation of the space $H_{\mathrm{curl},0}$:

$$H^h_{\mathrm{curl},0} = \left\{ \delta\mathbf{B} \,\middle|\, \delta\mathbf{B} = \sum_{jm} \left(\sum_{k=1}^{P} \sum_{\lambda=-1}^{1} \delta\mathbf{B}^{(\lambda)}_{jm,k} \psi_k \mathbf{S}^{(\lambda)}_{jm} + \delta B^{(-1)}_{jm,P+1} \psi_{P+1} \mathbf{S}^{(-1)}_{jm} \right) \right\}. \tag{56}$$

The Galerkin approximation of the solution of eqs (50)–(52) is then such a function ${}^{i+1}\mathbf{B} \in H^h{}_{\mathrm{curl}}$ that satisfies eq. (50) for all test functions $\delta\mathbf{B} \in H^h{}_{\mathrm{curl},0}$ and the boundary conditions (51)–(52) for $j = 1, \ldots, j_{\max}$, $m = 0, \ldots, j$.

Now we aim to derive the spherical harmonic-finite element approximations of the L_2 scalar product $(\cdot, \cdot)$, and of the sesquilinear forms $a_0(\cdot, \cdot)$ and $a_1(\cdot, \cdot)$. Because $\mathbf{B}$ is a real function, we can replace it by complex conjugation and make use of the orthogonality of the spherical harmonics (A8). Separating the radial and angular parts of the volume integral, $\int_G \mathrm{d}V = \int_0^a r^2\,\mathrm{d}r \int_\Omega \mathrm{d}\Omega$, and substituting for $\mathbf{B}$ and $\delta\mathbf{B}$ the basis functions $\psi_k(r)\,\mathbf{S}^{(\lambda)}_{jm}(\Omega)$, yields for the L_2 scalar product,

$$\left(\psi_k \overline{\mathbf{S}}^{(\lambda)}_{jm}, \psi_{k'} \mathbf{S}^{(\lambda')}_{j'm'}\right) = \delta_{jj'}\delta_{mm'}\delta_{\lambda\lambda'} N_{j\lambda} \left[I^{(2)}_k \delta_{k(k'-1)} + \left(I^{(1)}_k + I^{(3)}_{k-1} \right) \delta_{kk'} + I^{(2)}_{k-1} \delta_{k(k'+1)} \right]. \tag{57}$$

The norm $N_{j\lambda}$ is given by eq. (A9). In the previous equations, we have introduced the integrals of the finite element products over intervals $\mathcal{I}_k$, which can be expressed analytically:

$$I^{(1)}_k = \int_{r_k}^{r_{k+1}} \psi_k(r)\psi_k(r) r^2 \mathrm{d}r = \frac{h_k}{30}\left(r^2_{k+1} + 3r_k r_{k+1} + 6r^2_k\right), \tag{58}$$

$$I^{(2)}_k = \int_{r_k}^{r_{k+1}} \psi_k(r)\psi_{k+1}(r) r^2 \mathrm{d}r = \frac{h_k}{60}\left(3r^2_{k+1} + 4r_k r_{k+1} + 3r^2_k\right), \tag{59}$$

$$I^{(3)}_k = \int_{r_k}^{r_{k+1}} \psi_{k+1}(r)\psi_{k+1}(r) r^2 \mathrm{d}r = \frac{h_k}{30}\left(6r^2_{k+1} + 3r_k r_{k+1} + r^2_k\right). \tag{60}$$

These are defined for $k = 1, \ldots, P$. To keep unified notation of formula (57) even for the lowermost ($k, k' = 1$) and for the uppermost (k, $k' = P$) layers, we formally define $I^{(\cdot)}_0 = I^{(\cdot)}_{P+1} = 0$.

Before we express the approximation of the form $a_0(\cdot, \cdot)$, we define on each interval $\mathcal{I}_k$ functions

$$\chi_k(r) = r\left(\frac{d}{dr} + \frac{1}{r}\right)\psi_k(r) = \frac{r_{k+1} - 2r}{h_k}, \tag{61}$$

$$\chi_{k+1}(r) = r\left(\frac{d}{dr} + \frac{1}{r}\right)\psi_{k+1}(r) = \frac{2r - r_k}{h_k}. \tag{62}$$

Then, using eqs (A16)–(A18), we can write the rotation of the basis functions $\psi_k \overline{\mathbf{S}}^{(\lambda)}_{jm}$ from $H^h_{\rm curl}$ as

$$r\,\mathrm{curl}\left[\psi_k(r)\mathbf{S}^{(0)}_{jm}(\Omega)\right] = -\Pi_j\,\psi_k(r)\mathbf{S}^{(-1)}_{jm}(\Omega) - \chi_k(r)\mathbf{S}^{(1)}_{jm}(\Omega), \tag{63}$$

$$r\,\mathrm{curl}\left[\psi_k(r)\mathbf{S}^{(-1)}_{jm}(\Omega)\right] = -\psi_k(r)\mathbf{S}^{(0)}_{jm}(\Omega), \tag{64}$$

$$r\,\mathrm{curl}\left[\psi_k(r)\mathbf{S}^{(1)}_{jm}(\Omega)\right] = \chi_k(r)\mathbf{S}^{(0)}_{jm}(\Omega), \tag{65}$$

where Π_j is defined in eq. (A10). Introducing the piecewise constant parametrization of the radial resistivity profile $\rho_0(r)$,

$$\rho_0(r) = \rho_{0,k} = \text{const} \quad \text{for}\, r \in \mathcal{I}_k \tag{66}$$

and substituting eqs (63)–(65) into the definition (47), yields for the form $a_0(\cdot,\cdot)$,

$$\begin{aligned} a_0\left(\psi_k\overline{\mathbf{S}}^{(\lambda)}_{jm}, \psi_{k'}\mathbf{S}^{(0)}_{j'm'}\right) &= \delta_{jj'}\delta_{mm'}\delta_{\lambda 0}\Pi_j\Big[\left(\Pi_j K^{(2)}_k + K^{(5)}_k\right)\rho_{0,k}\delta_{k(k'-1)} \\ &\quad + \left(\Pi_j K^{(3)}_{k-1} + K^{(6)}_{k-1}\right)\rho_{0,k-1}\delta_{kk'} + \left(\Pi_j K^{(1)}_k + K^{(4)}_k\right)\rho_{0,k}\delta_{kk'} + \left(\Pi_j K^{(2)}_{k-1} + K^{(5)}_{k-1}\right)\rho_{0,k-1}\delta_{k(k'+1)}\Big], \end{aligned} \tag{67}$$

$$\begin{aligned} a_0\left(\psi_k\overline{\mathbf{S}}^{(\lambda)}_{jm}, \psi_{k'}\mathbf{S}^{(-1)}_{j'm'}\right) &= \delta_{jj'}\delta_{mm'}\delta_{\lambda -1}\Pi_j\left(K^{(2)}_k\rho_{0,k}\delta_{k(k'-1)} + K^{(3)}_{k-1}\rho_{0,k-1}\delta_{kk'} + K^{(1)}_k\rho_{0,k}\delta_{kk'} + K^{(2)}_{k-1}\rho_{0,k-1}\delta_{k(k'+1)}\right) \\ &\quad - \delta_{jj'}\delta_{mm'}\delta_{\lambda 1}\Pi_j\left(K^{(8)}_k\rho_{0,k}\delta_{k(k'-1)} + K^{(10)}_{k-1}\rho_{0,k-1}\delta_{kk'} + K^{(7)}_k\rho_{0,k}\delta_{kk'} + K^{(9)}_{k-1}\rho_{0,k-1}\delta_{k(k'+1)}\right), \end{aligned} \tag{68}$$

$$\begin{aligned} a_0\left(\psi_k\overline{\mathbf{S}}^{(\lambda)}_{jm}, \psi_{k'}\mathbf{S}^{(1)}_{j'm'}\right) &= -\delta_{jj'}\delta_{mm'}\delta_{\lambda -1}\Pi_j\left(K^{(9)}_k\rho_{0,k}\delta_{k(k'-1)} + K^{(10)}_{k-1}\rho_{0,k-1}\delta_{kk'} + K^{(7)}_k\rho_{0,k}\delta_{kk'} + K^{(8)}_{k-1}\rho_{0,k-1}\delta_{k(k'+1)}\right) \\ &\quad + \delta_{jj'}\delta_{mm'}\delta_{\lambda 1}\Pi_j\left(K^{(5)}_k\rho_{0,k}\delta_{k(k'-1)} + K^{(6)}_{k-1}\rho_{0,k-1}\delta_{kk'} + K^{(4)}_k\rho_{0,k}\delta_{kk'} + K^{(5)}_{k-1}\rho_{0,k-1}\delta_{k(k'+1)}\right). \end{aligned} \tag{69}$$

We have introduced additional integrals over $\mathcal{I}_k$, namely,

$$K^{(1)}_k = \int_{r_k}^{r_{k+1}} \psi_k(r)\psi_k(r)\,\mathrm{d}r = \frac{h_k}{3}, \tag{70}$$

$$K^{(2)}_k = \int_{r_k}^{r_{k+1}} \psi_k(r)\psi_{k+1}(r)\,\mathrm{d}r = \frac{h_k}{6}, \tag{71}$$

$$K^{(3)}_k = \int_{r_k}^{r_{k+1}} \psi_{k+1}(r)\psi_{k+1}(r)\,\mathrm{d}r = \frac{h_k}{3}, \tag{72}$$

$$K^{(4)}_k = \int_{r_k}^{r_{k+1}} \chi_k(r)\chi_k(r)\,\mathrm{d}r = \frac{1}{3\,h_k}\left(r^2_{k+1} - 2r_{k+1}r_k + 4r^2_k\right), \tag{73}$$

$$K^{(5)}_k = \int_{r_k}^{r_{k+1}} \chi_k(r)\chi_{k+1}(r)\,\mathrm{d}r = -\frac{1}{3\,h_k}\left(r^2_{k+1} + r_{k+1}r_k + r^2_k\right), \tag{74}$$

$$K^{(6)}_k = \int_{r_k}^{r_{k+1}} \chi_{k+1}(r)\chi_{k+1}(r)\,\mathrm{d}r = \frac{1}{3\,h_k}\left(4r^2_{k+1} - 2r_{k+1}r_k + r^2_k\right), \tag{75}$$

$$K^{(7)}_k = \int_{r_k}^{r_{k+1}} \psi_k(r)\chi_k(r)\,\mathrm{d}r = \frac{1}{6}\left(r_{k+1} - 4r_k\right), \tag{76}$$

$$K^{(8)}_k = \int_{r_k}^{r_{k+1}} \psi_{k+1}(r)\chi_k(r)\,\mathrm{d}r = -\frac{1}{6}\left(r_{k+1} + 2r_k\right), \tag{77}$$

$$K^{(9)}_k = \int_{r_k}^{r_{k+1}} \psi_k(r)\chi_{k+1}(r)\,\mathrm{d}r = \frac{1}{6}\left(2r_{k+1} + r_k\right), \tag{78}$$

$$K_k^{(10)} = \int_{r_k}^{r_{k+1}} \psi_{k+1}(r)\chi_{k+1}(r)\,\mathrm{d}r = \frac{1}{6}\,(4r_{k+1} - r_k)\,, \tag{79}$$

for $k = 1, \ldots, P$. Analogously to $I_k^{(\cdot)}$, we formally define $K_0^{(\cdot)} = K_{P+1}^{(\cdot)} = 0$.

Note that both the L_2 scalar product and the form $a_0(\cdot, \cdot)$ are decoupled in indices j and m, and the coupling in the index k is limited to neighbouring layers. The former is not valid in the approximation of the form $a_1(\cdot, \cdot)$ (eq. 48), where lateral variations of ρ_1 introduce coupling in j and m. In the evaluation of $a_1(\cdot, \cdot)$, we follow generally the technique developed by Martinec (1999) with minor modifications as a result of our choice of a different system of vector spherical harmonics.

We prescribe the resistivity variations on an angular grid of $N_\vartheta \times N_\varphi$ nodes and piecewise constant with respect to the radial coordinate, i.e.

$$\rho_1(r, \vartheta_p, \varphi_q) = \rho_{1,k}^{pq} = \text{const} \quad \text{for } r \in \mathcal{I}_k, \tag{80}$$

where colatitudinal grid nodes $\{\vartheta_p\}_{p=1}^{N_\vartheta}$ are the roots of Legendre polynomial of degree N_ϑ,

$$P_{N_\vartheta}(\cos\vartheta_p) = 0, \tag{81}$$

and longitudinal grid nodes $\{\varphi_q\}_{q=0}^{N_\varphi - 1}$ are equidistant,

$$\varphi_q = \frac{2\pi q}{N_\varphi}. \tag{82}$$

Moreover, we require that $N_\vartheta > 3j_{\max}/2$, $N_\varphi > 3j_{\max}$ and N_φ is an integer power of 2 (Martinec 1989).

Now we define the following sums on the grid (ϑ_p, φ_q) and for all radial indices $k = 1, \ldots, P + 1$,

$$Q_{pq,k}^{(1)} = \sum_{jm} \Pi_j\, {}^i\overline{B}_{jm,k}^{(0)}\, \overline{Y}_{jm}(\vartheta_p, \varphi_q), \tag{83}$$

$$Q_{pq,k}^{(2)} = \sum_{jm} {}^i\overline{B}_{jm,k}^{(0)}\, \frac{\partial \overline{Y}_{jm}}{\partial \vartheta}(\vartheta_p, \varphi_q), \tag{84}$$

$$Q_{pq,k}^{(3)} = \sum_{jm} {}^i\overline{B}_{jm,k}^{(0)}\, \frac{1}{\sin\vartheta_p}\, \frac{\partial \overline{Y}_{jm}}{\partial \varphi}(\vartheta_p, \varphi_q), \tag{85}$$

$$Q_{pq,k}^{(4)} = \sum_{jm} {}^i\overline{B}_{jm,k}^{(-1)}\, \frac{\partial \overline{Y}_{jm}}{\partial \vartheta}(\vartheta_p, \varphi_q), \tag{86}$$

$$Q_{pq,k}^{(5)} = \sum_{jm} {}^i\overline{B}_{jm,k}^{(-1)}\, \frac{1}{\sin\vartheta_p}\, \frac{\partial \overline{Y}_{jm}}{\partial \varphi}(\vartheta_p, \varphi_q), \tag{87}$$

$$Q_{pq,k}^{(6)} = \sum_{jm} {}^i\overline{B}_{jm,k}^{(1)}\, \frac{\partial \overline{Y}_{jm}}{\partial \vartheta}(\vartheta_p, \varphi_q), \tag{88}$$

$$Q_{pq,k}^{(7)} = \sum_{jm} {}^i\overline{B}_{jm,k}^{(1)}\, \frac{1}{\sin\vartheta_p}\, \frac{\partial \overline{Y}_{jm}}{\partial \varphi}(\vartheta_p, \varphi_q). \tag{89}$$

Because of the exponential function $\exp(-im\varphi_q)$ in the spherical harmonic functions $\overline{Y}_{jm}$, the summation over m for each node φ_q can be computed by the Fast Fourier Transform (FFT) algorithm (Martinec 1989; Press *et al.* 1992, p. 498).

The sums $Q_{pq,k}^{(\alpha)}$ are then multiplied by discretized resistivity and spherical harmonics, or their angular derivatives, and numerically integrated over the angular coordinates,

$$C_{jm,k}^{(11)} = \frac{2\pi}{N_\varphi}\Pi_j \sum_{p=1}^{N_\vartheta}\sum_{q=0}^{N_\varphi - 1} w_p \rho_{1,k}^{pq} Q_{pq,k}^{(1)} Y_{jm}(\vartheta_p, \varphi_q), \tag{90}$$

$$C_{jm,k}^{(\alpha 2)} = \frac{2\pi}{N_\varphi} \sum_{p=1}^{N_\vartheta}\sum_{q=0}^{N_\varphi - 1} w_p \rho_{1,k}^{pq} Q_{pq,k}^{(\alpha)} \frac{\partial Y_{jm}}{\partial \vartheta}(\vartheta_p, \varphi_q), \tag{91}$$

$$C_{jm,k}^{(\alpha 3)} = \frac{2\pi}{N_\varphi} \sum_{p=1}^{N_\vartheta}\sum_{q=0}^{N_\varphi - 1} w_p \rho_{1,k}^{pq} Q_{pq,k}^{(\alpha)} \frac{1}{\sin\vartheta_p} \frac{\partial Y_{jm}}{\partial \varphi}(\vartheta_p, \varphi_q), \tag{92}$$

$$D_{jm,k}^{(11)} = \frac{2\pi}{N_\varphi}\Pi_j \sum_{p=1}^{N_\vartheta}\sum_{q=0}^{N_\varphi - 1} w_p \rho_{1,k}^{pq} Q_{pq,k+1}^{(1)} Y_{jm}(\vartheta_p, \varphi_q), \tag{93}$$

$$D^{(\alpha 2)}_{jm,k} = \frac{2\pi}{N_\varphi} \sum_{p=1}^{N_\vartheta} \sum_{q=0}^{N_\varphi - 1} w_p \rho^{pq}_{1,k} Q^{(\alpha)}_{pq,k+1} \frac{\partial Y_{jm}}{\partial \vartheta}(\vartheta_p, \varphi_q), \tag{94}$$

$$D^{(\alpha 3)}_{jm,k} = \frac{2\pi}{N_\varphi} \sum_{p=1}^{N_\vartheta} \sum_{q=0}^{N_\varphi - 1} w_p \rho^{pq}_{1,k} Q^{(\alpha)}_{pq,k+1} \frac{1}{\sin\vartheta_p} \frac{\partial Y_{jm}}{\partial \varphi}(\vartheta_p, \varphi_q), \tag{95}$$

for all $j = 1, \ldots, j_{\max}$, $m = 0, \ldots, j$ and $k = 1, \ldots, P$. Index α ranges from 2 to 7. In the previous equations, we employed the Gauss–Legendre formula with weights w_p (Press *et al.* 1992, p. 140) for numerical integration over ϑ,

$$\int_0^\pi f(\vartheta) \sin\vartheta \, \mathrm{d}\vartheta \approx \sum_{p=1}^{N_\vartheta} w_p f(\vartheta_p), \tag{96}$$

and the discrete FFT over φ,

$$\int_0^{2\pi} f(\varphi) e^{im\varphi} \mathrm{d}\varphi \approx \frac{2\pi}{N_\varphi} \sum_{q=1}^{N_\varphi - 1} f(\varphi_q) e^{im\varphi_q}. \tag{97}$$

Note that the coefficients $C^{(\alpha\beta)}_{jm,k}$ and $D^{(\alpha\beta)}_{jm,k}$ are identically zero if the kth layer is homogeneous, i.e. if $\rho^{pq}_{1,k} = 0$. Then skipping the summations (83)–(95) saves a considerable amount of CPU time. This can be practical for conductivity models where the lateral variations are confined only to several layers and the rest of the model is spherically symmetric.

The spherical harmonic-finite element approximation of the form $a_1(\cdot, \cdot)$ then can be evaluated for each basis function from $H^h{}_{\mathrm{curl},0}$ by combining the angular integrals (90)–(95) with the radial integrals (70)–(79) and taking into account the rotation formulae (63)–(65):

$$\begin{aligned}
a_1\left({}^i\mathbf{B}, \psi_k \mathbf{S}^{(0)}_{jm}\right) = {} & \left(C^{(11)}_{jm,k-1} K^{(2)}_{k-1} + D^{(11)}_{jm,k-1} K^{(3)}_{k-1} + C^{(11)}_{jm,k} K^{(1)}_k + D^{(11)}_{jm,k} K^{(2)}_k\right) \\
& + \left(C^{(22)}_{jm,k-1} K^{(5)}_{k-1} + D^{(22)}_{jm,k-1} K^{(6)}_{k-1} + C^{(22)}_{jm,k} K^{(4)}_k + D^{(22)}_{jm,k} K^{(5)}_k\right) \\
& + \left(C^{(33)}_{jm,k-1} K^{(5)}_{k-1} + D^{(33)}_{jm,k-1} K^{(6)}_{k-1} + C^{(33)}_{jm,k} K^{(4)}_k + D^{(33)}_{jm,k} K^{(5)}_k\right) \\
& + \left(C^{(43)}_{jm,k-1} K^{(9)}_{k-1} + D^{(43)}_{jm,k-1} K^{(10)}_{k-1} + C^{(43)}_{jm,k} K^{(7)}_k + D^{(43)}_{jm,k} K^{(8)}_k\right) \\
& - \left(C^{(52)}_{jm,k-1} K^{(9)}_{k-1} + D^{(52)}_{jm,k-1} K^{(10)}_{k-1} + C^{(52)}_{jm,k} K^{(7)}_k + D^{(52)}_{jm,k} K^{(8)}_k\right) \\
& - \left(C^{(63)}_{jm,k-1} K^{(5)}_{k-1} + D^{(63)}_{jm,k-1} K^{(6)}_{k-1} + C^{(63)}_{jm,k} K^{(4)}_k + D^{(63)}_{jm,k} K^{(5)}_k\right) \\
& + \left(C^{(72)}_{jm,k-1} K^{(5)}_{k-1} + D^{(72)}_{jm,k-1} K^{(6)}_{k-1} + C^{(72)}_{jm,k} K^{(4)}_k + D^{(72)}_{jm,k} K^{(5)}_k\right),
\end{aligned} \tag{98}$$

$$\begin{aligned}
a_1\left({}^i\mathbf{B}, \psi_k \mathbf{S}^{(-1)}_{jm}\right) = {} & \left(C^{(32)}_{jm,k-1} K^{(8)}_{k-1} + D^{(32)}_{jm,k-1} K^{(10)}_{k-1} + C^{(32)}_{jm,k} K^{(7)}_k + D^{(32)}_{jm,k} K^{(9)}_k\right) \\
& - \left(C^{(23)}_{jm,k-1} K^{(8)}_{k-1} + D^{(23)}_{jm,k-1} K^{(10)}_{k-1} + C^{(23)}_{jm,k} K^{(7)}_k + D^{(23)}_{jm,k} K^{(9)}_k\right) \\
& + \left(C^{(42)}_{jm,k-1} K^{(2)}_{k-1} + D^{(42)}_{jm,k-1} K^{(3)}_{k-1} + C^{(42)}_{jm,k} K^{(1)}_k + D^{(42)}_{jm,k} K^{(2)}_k\right) \\
& + \left(C^{(53)}_{jm,k-1} K^{(2)}_{k-1} + D^{(53)}_{jm,k-1} K^{(3)}_{k-1} + C^{(53)}_{jm,k} K^{(1)}_k + D^{(53)}_{jm,k} K^{(2)}_k\right) \\
& - \left(C^{(62)}_{jm,k-1} K^{(8)}_{k-1} + D^{(62)}_{jm,k-1} K^{(10)}_{k-1} + C^{(62)}_{jm,k} K^{(7)}_k + D^{(62)}_{jm,k} K^{(9)}_k\right) \\
& - \left(C^{(73)}_{jm,k-1} K^{(8)}_{k-1} + D^{(73)}_{jm,k-1} K^{(10)}_{k-1} + C^{(73)}_{jm,k} K^{(7)}_k + D^{(73)}_{jm,k} K^{(9)}_k\right),
\end{aligned} \tag{99}$$

$$\begin{aligned}
a_1\left({}^i\mathbf{B}, \psi_k \mathbf{S}^{(1)}_{jm}\right) = {} & \left(C^{(23)}_{jm,k-1} K^{(5)}_{k-1} + D^{(23)}_{jm,k-1} K^{(6)}_{k-1} + C^{(23)}_{jm,k} K^{(4)}_k + D^{(23)}_{jm,k} K^{(5)}_k\right) \\
& - \left(C^{(32)}_{jm,k-1} K^{(5)}_{k-1} + D^{(32)}_{jm,k-1} K^{(6)}_{k-1} + C^{(32)}_{jm,k} K^{(4)}_k + D^{(32)}_{jm,k} K^{(5)}_k\right) \\
& - \left(C^{(42)}_{jm,k-1} K^{(9)}_{k-1} + D^{(42)}_{jm,k-1} K^{(10)}_{k-1} + C^{(42)}_{jm,k} K^{(7)}_k + D^{(42)}_{jm,k} K^{(8)}_k\right) \\
& - \left(C^{(53)}_{jm,k-1} K^{(9)}_{k-1} + D^{(53)}_{jm,k-1} K^{(10)}_{k-1} + C^{(53)}_{jm,k} K^{(7)}_k + D^{(53)}_{jm,k} K^{(8)}_k\right) \\
& + \left(C^{(62)}_{jm,k-1} K^{(5)}_{k-1} + D^{(62)}_{jm,k-1} K^{(6)}_{k-1} + C^{(62)}_{jm,k} K^{(4)}_k + D^{(62)}_{jm,k} K^{(5)}_k\right) \\
& + \left(C^{(73)}_{jm,k-1} K^{(5)}_{k-1} + D^{(73)}_{jm,k-1} K^{(6)}_{k-1} + C^{(73)}_{jm,k} K^{(4)}_k + D^{(73)}_{jm,k} K^{(5)}_k\right).
\end{aligned} \tag{100}$$

Let us order the unknown coefficients ${}^{i+1}\overline{B}^{(\lambda)}_{jm,k}$ of the magnetic field at the $(i+1)$th time step into a complex column vector

$$\mathbf{x}^T = \left\{ \left[\left({}^{i+1}\overline{B}^{(k)}_{jm,k}, {}^{i+1}\overline{B}^{(-1)}_{jm,k}, {}^{i+1}\overline{B}^{(1)}_{jm,k} \right)_{k=1}^{P+1} \right]_{m=0}^{j} \right\}_{j=1}^{j_{\max}}, \tag{101}$$

with dimension $d = 3(P+1)j_{\max}(j_{\max}+3)/2$. The complex coefficients for negative m are not included in vector $\mathbf{x}$, but, when needed in the evaluation of $a_1(\cdot,\cdot)$, they are computed using the symmetry (55). Now we construct the Galerkin system of d linear complex equations, which represents a discrete approximation of eqs (50)–(52),

$$\mathbf{A}\cdot\mathbf{x} = \mathbf{y}. \tag{102}$$

The elements of matrix $\mathbf{A}$ and the right-hand side vector $\mathbf{y}$ are defined as

$$a_{n'n} = \frac{\mu_0}{\Delta t}\left(\psi_k \overline{\mathbf{S}}^{(\lambda)}_{jm}, \psi_{k'}\mathbf{S}^{(\lambda')}_{j'm'}\right) + a_0\left(\psi_k \overline{\mathbf{S}}^{(\lambda)}_{jm}, \psi_{k'}\mathbf{S}^{(\lambda')}_{j'm'}\right), \tag{103}$$

$$y_{n'} = \frac{\mu_0}{\Delta t}\sum_{j=1}^{j_{\max}}\sum_{m=-j}^{j}\sum_{k=1}^{P+1}\sum_{\lambda=-1}^{1} {}^{i}\overline{B}^{(\lambda)}_{jm,k}\left(\psi_k \overline{\mathbf{S}}^{(\lambda)}_{jm}, \psi_{k'}\mathbf{S}^{(\lambda')}_{j'm'}\right) - a_1\left({}^{i}\mathbf{B}, \psi_{k'}\mathbf{S}^{(\lambda')}_{j'm'}\right), \tag{104}$$

where the multi-indices n and n' are considered from intervals

$$n = \{j, m, k, \lambda\} = \{\{1,\ldots,j_{\max}\}, \{0,\ldots,j\}, \{1,\ldots,P+1\}, \{0,-1,1\}\}, \tag{105}$$

$$n' = \{j', m', k', \lambda'\} = \left\{\{1,\ldots,j_{\max}\}, \{0,\ldots,j'\}, \{1,\ldots,P+\delta_{\lambda'-1}\}, \{0,-1,1\}\right\}. \tag{106}$$

Because the test functions $\psi_{P+1}\overline{\mathbf{S}}^{(0)}_{jm}$ and $\psi_{P+1}\overline{\mathbf{S}}^{(1)}_{jm}$ were excluded from $H^h{}_{\mathrm{curl},0}$, there are two missing equations for each $j'm'$ in eqs (103)–(106). Hence, the system must be completed by the boundary conditions (24)–(25). The constraint on the toroidal field on the surface ∂G is imposed by prescribing

$$a_{n'n} = \delta_{jj'}\delta_{mm'}\delta_{k(P+1)}\delta_{\lambda 0}, \quad y_{n'} = 0, \tag{107}$$

for $n' = \left\{\{1,\ldots,j_{\max}\}, \{0,\ldots,j'\}, P+1, 0\right\}$. The load by external magnetic potential is implemented by setting

$$a_{n'n} = \delta_{jj'}\delta_{mm'}\delta_{k(P+1)}\left[(\delta_{\lambda-1} + (j+1)\delta_{\lambda 1}\right], \quad y_{n'} = -(2j'+1)\overline{G}^{(e)}_{j'm'}(t_{i+1}),$$

for $n' = \left\{\{1,\ldots,j_{\max}\}, \{0,\ldots,j'\}, P+1, 1\right\}$. (108)

Matrix $\mathbf{A}$ is a complex nine-banded matrix, which depends only on the length of the time step Δt and on the radial resistivity structure ρ_0. Because the linear system (102) is repeatedly solved in each time step, it is effective to use the lower-upper (LU) triangle decomposition of $\mathbf{A}$. Using a subroutine provided by LAPACK (Anderson *et al.* 1999), for $j_{\max} = 40$ and $P = 100$, it takes only about 10 s on a 500-MHz PC to decompose $\mathbf{A}$. Evaluation of the right-hand side $\mathbf{y}$ is based on eqs (83)–(95) and (98)–(100), and uses the solution ${}^{i}\mathbf{B}$ from the previous time step. It is the most time-consuming part of the algorithm and takes approximately 20 s for each time step at given spatial resolution.

3 VALIDATION

3.1 Nested-sphere conductivity models

In this section, we validate the presented time-domain spherical harmonic-finite element (from now on denoted as TD) approach using the conductivity models consisting of a homogeneous sphere with a nested spherical inclusion of different conductivity. The configuration of the nested-sphere conductivity model is shown in Fig. 3. This class of models, with a frequency-domain, semi-analytical (SA) solution developed by Everett & Schultz (1995) for axially symmetric models and generalized by Martinec (1998) to treat an off-axis spherical inclusion, has become a standard tool for validation of 3-D EM forward solvers (Everett & Schultz 1996; Martinec 1999; Uyeshima & Schultz 2000).

In each homogeneous sphere, the equation of EM induction reduces to a complex vector Helmholtz equation, $(\nabla^2 + k_n^2)\,\mathbf{B}_{\mathrm{SA}} = 0$, where $k_n^2 = -i\omega\mu_0\sigma_n$. The magnetic induction vector $\mathbf{B}_{\mathrm{SA}}$ is expanded into truncated series of eigenfunctions of the Helmholtz operator. The coefficients of the expansion in both spheres are determined from the boundary conditions on the interface by solving a system of linear equations.

Although theoretically this method should provide results of almost analytical accuracy, caution must be paid when using a high-degree spherical harmonic expansion for high frequencies ω, where the method often breaks down numerically. However, this numerical instability has a physical background. As the frequency ω increases, the penetration depth of the damped EM wave decreases, and the solution becomes less sensitive to the position, size and conductivity of the inclusion. For $\omega \to \infty$, the response of the nested-spheres model converges to the response of a homogeneous sphere. In the case of dipolar excitation, the response of a homogeneous sphere can be expressed by dipolar terms only. Therefore, the truncation degree $j_{\max}$ for a particular frequency band is chosen according to two criteria. First, $j_{\max}$ is small enough to yield a stable solution, i.e. the power of magnetic field is a decreasing function of spherical harmonic degree j. Secondly, $j_{\max}$ is large enough to parametrize the model sufficiently, i.e. introducing small variations of $j_{\max}$ in both directions has no significant impact on the obtained solution.

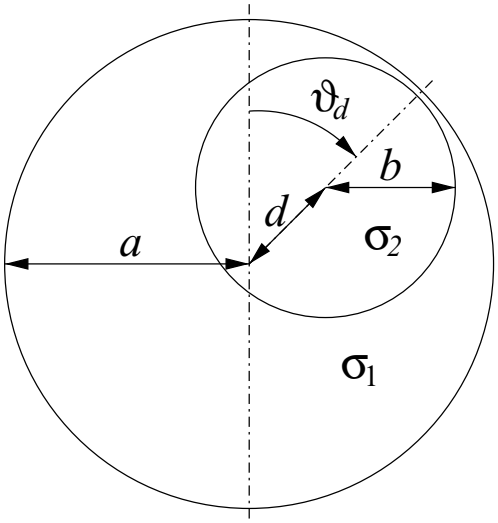

Figure 3. Nested-sphere conductivity model (cross-section). A homogeneous sphere with radius b and conductivity σ_2 is nested in the host sphere with radius a and conductivity σ_1. The centre of the inclusion is positioned at a distance d from the centre of the host sphere at colatitude ϑ_d and longitude φ_d.

We use the following models in the validation. In model A, the host sphere with radius $a = 6371$ km has conductivity $\sigma_1 = 1$ S m^{-1}. The centre of the spherical inclusion with radius $b = 3500$ km and conductivity $\sigma_2 = 10$ S m^{-1} is positioned at a distance $d = 2700$ km from the centre of the host sphere at colatitude $\vartheta_d = 40^\circ$ and longitude $\varphi_d = 35^\circ$. In models B and C, the conductivity of the host sphere is decreased to $\sigma_1 = 0.1$ S m^{-1} and the conductivity of the inclusion is respectively set to $\sigma_2 = 10$ S m^{-1} and $\sigma_2 = 1$ S m^{-1}, yielding the conductivity contrasts of 2 and 1 order of magnitude.

3.2 Excitation

The presented method allows the excitation by an arbitrary spatiotemporal configuration of the external inducing field. In the following examples, we excite the conductivity models by two different types of signal.

In order to compare the results in the frequency domain, we use harmonic signals (denoted as loads 1a, 1b, 1c from now on) with simple dipolar spatial structure,

$$G^{(e)}_{jm}(t) = \begin{cases} A\sqrt{\frac{4\pi}{3}}\sin(\omega_{a,b,c}t) & \text{for } j = 1, m = 0, \\ 0 & \text{otherwise,} \end{cases} \tag{109}$$

where $A = 100$ nT is the amplitude and $\sqrt{4\pi/3}$ is the inverse norm of $P_{10}(\cos\vartheta)$. We use the following angular frequencies: $\omega_a = 3 \times 10^{-7}$ rad s^{-1} (corresponding to period $T_a = 242$ d), $\omega_b = 2.7 \times 10^{-6}$ rad s^{-1} ($T_b = 27$ d), and $\omega_c = 8.08 \times 10^{-6}$ rad s^{-1} ($T_c = 9$ d). Frequency ω_a is unusually low for induction studies. It assures that the EM energy penetrates down to the centre of the sphere, allowing to test the 3-D method throughout the model. Frequencies ω_b and ω_c are typical for frequency-domain Dst studies.

The second model (load 2) of the excitation source used for validation of the TD approach is an analytical approximation of the complicated spatiotemporal structure of a geomagnetic storm (Daglis & Kozyra 2002; Everett & Martinec 2003). We define a time-varying dipolar coefficient of the external magnetic potential as

$$G^{(e)}_{jm}(t) = \begin{cases} A\sqrt{\frac{4\pi}{3}}te^{-\alpha t} & \text{for } j = 1, m = 0, \\ 0 & \text{otherwise,} \end{cases} \tag{110}$$

where $A = 0.003$ nT s^{-1} is the amplitude and $1/\alpha = 48$ h is relaxation time of the storm. Regardless of its simplicity, this mathematical model characterizes two basic features of magnetic storms, the P_{10} spatial configuration, and the time evolution with relatively fast onset and slow relaxation (see Fig. 4). The Fourier spectrum of signal from eq. (110) has the analytical form (Martinec *et al.* 2003),

$$\hat{G}^{(e)}_{10}(\omega) = \sqrt{\frac{4\pi}{3}}\frac{A}{2\pi}\frac{\alpha^2 - \omega^2 - 2i\alpha\omega}{(\alpha^2 + \omega^2)^2}. \tag{111}$$

3.3 Results

In the first set of tests, we validate the TD approach in the frequency domain. The time-domain integration is started from the zero initial condition. The corresponding transient switch-on effect is incompatible with the infinite harmonic signal. However, if we let evolve the solution

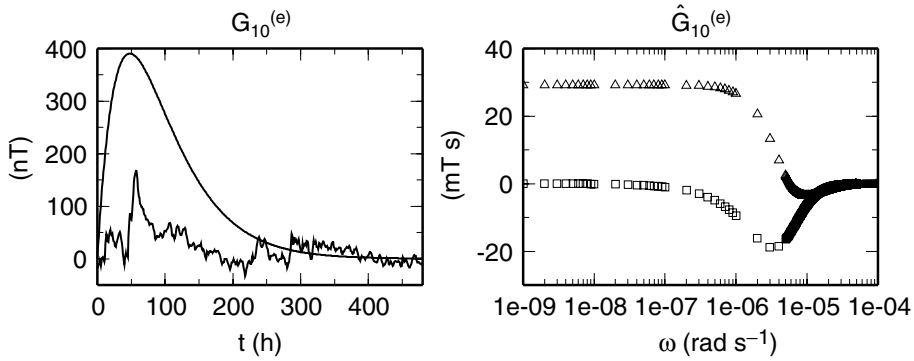

Figure 4. Analytical model of the geomagnetic storm defined by eq. (110) is shown in the left panel. The $G_{10}^{(e)}$ coefficient derived from the disturbed (Dst) index during a real storm in 1980 February is plotted only for comparison. The Fourier spectrum of the analytical model is shown in the right panel with sampling that is used in the semi-analytical (SA) method. Open and solid symbols correspond to truncation degree of 18 and 12, respectively.

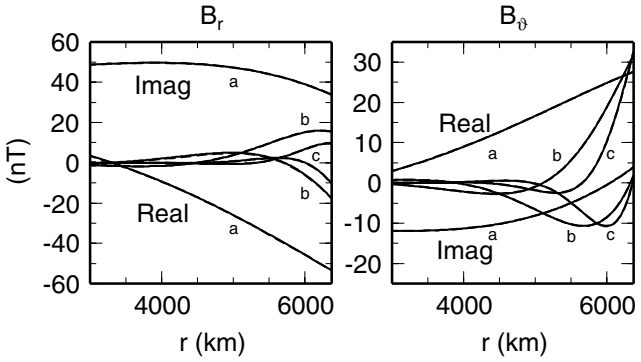

Figure 5. Magnetic induction vector **B** in a homogeneous sphere with unit conductivity excited by harmonic loads 1a, 1b and 1c. The components of **B** are plotted along radius at fixed colatitude $\vartheta = 13^\circ$ and longitude $\varphi = 0^\circ$. B_φ is identically zero. Solutions by time-domain spherical harmonic-finite element (TD) method with spatiotemporal discretization set to ($j_{\max}$, P, Δt) = (1, 100, 1 h) are plotted by dashed lines, analytical solutions (Everett & Martinec 2003) are plotted by solid lines.

for some time, the effect of the initial value will be damped exponentially and the TD solution starts to behave harmonically. In the presented examples, we run the time integration for at least four periods and then use only the last period to determine the frequency-domain response by evaluating the Fourier integral.

We start with a homogeneous sphere with conductivity $\sigma = 1$ S m^{-1} for which an analytical solution exists (Everett & Martinec 2003). The sphere is excited by harmonic loads 1a, 1b and 1c. Fig. 5 shows that the solutions obtained by the TD method agree perfectly with analytical solutions. Because there are no lateral conductivity variations, we have $\rho_1 = 0$, $a_1(\cdot, \cdot) = 0$ and the time-integration scheme becomes fully implicit. It also implies that no energy leaks to high-degree spherical harmonics and for P_{10} excitation it is sufficient to truncate the harmonic expansion at $j_{\max} = 1$.

In the next example, the nested-sphere model A is excited by the harmonic loads 1a, 1b and 1c. The configuration with long-periodic load 1a is not very realistic, but we investigate it rather thoroughly because it was used also by Everett & Schultz (1996) and Martinec (1999) and the results can be directly compared. Fig. 6 shows the convergence of the TD solution to the SA reference results as the spatial and temporal resolution increases. To improve readability, we plot only the anomalous field, i.e. the solution for the homogeneous sphere shown in Fig. 5 is subtracted from the results. The response of the nested-sphere model to a slowly varying, long-periodic signal is modelled with sufficient accuracy even by the runs with intermediate spatial and temporal resolution. The time integration is stable even for the 24-h time step, however, the differences from the SA solution in all three components of **B** increase with Δt. The SA solution is truncated at $j_{\max} = 18$. The spectral-finite element (SFE) solution by Martinec (1999) is also plotted in the bottom row of Fig. 6 for comparison. It uses the same spatial parametrization as the presented TD method and at high-resolution settings ($j_{\max}$, P) = (40, 100) shows similar accuracy.

Stability of the time integration can be also seen from Fig. 7. In the left plate, we display the time evolution of the errors with respect to the reference solution $\mathbf{B}_{\rm SA}$ at various resolutions. We define the error by formula

$$e(t) = 100\% \times \frac{||\mathbf{B}(t) - \mathbf{B}_{\rm SA}(t)||_{L_2(\partial G)}}{\left\langle ||\mathbf{B}_{\rm SA}||_{L_2(\partial G)} \right\rangle}, \tag{112}$$

where

$$\langle f \rangle = \frac{1}{T} \int_0^T f(t)\, {\rm d}t. \tag{113}$$

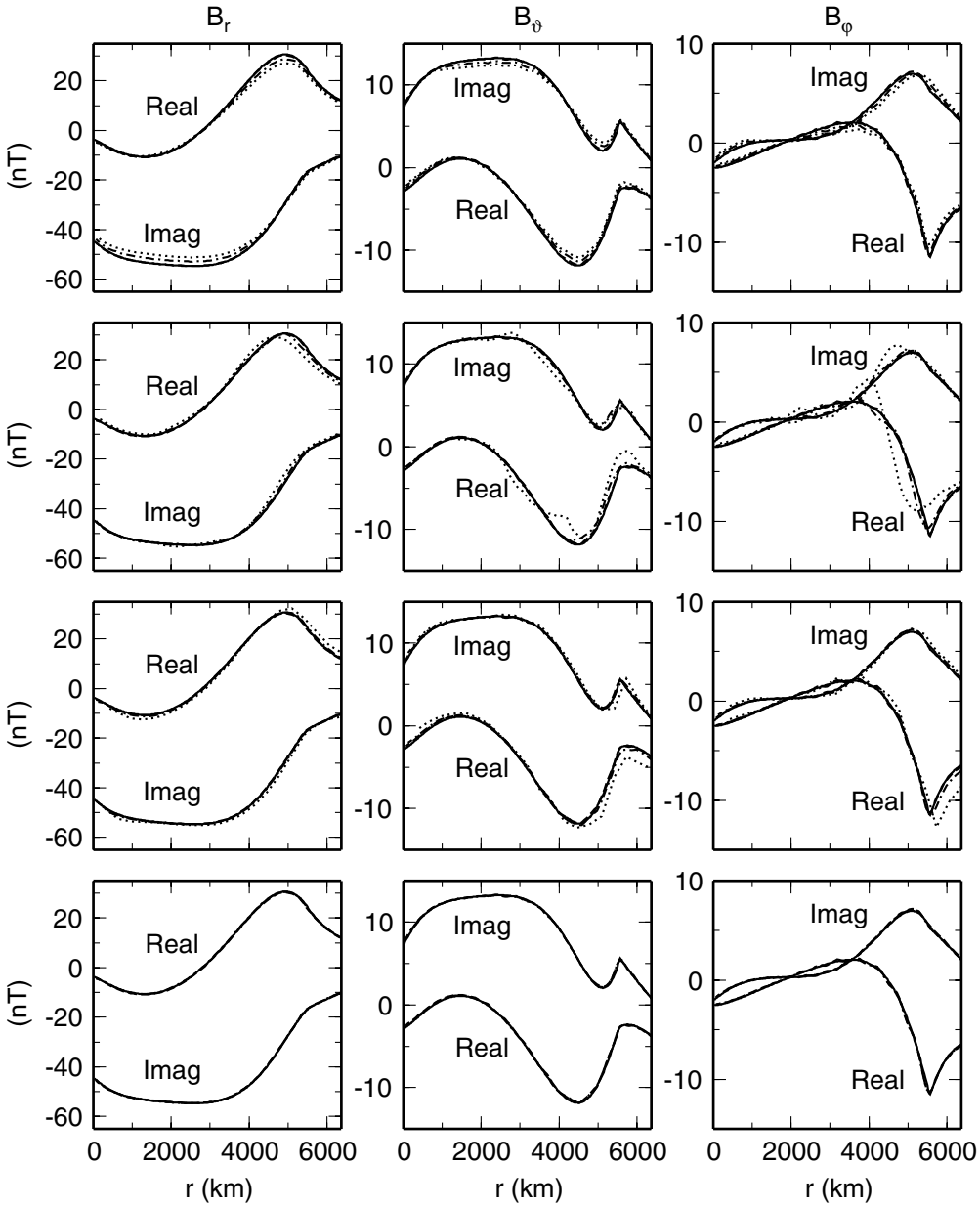

Figure 6. Resolution-dependent convergence of the time-domain spherical harmonic-finite element (TD) method towards the semi-analytical (SA) solution for the conductivity model A excited by load 1a. The components of **B** are plotted along radius at fixed colatitude $\vartheta = 13^\circ$ and longitude $\varphi = 0^\circ$. Only the differences with respect to the homogeneous sphere solution (Fig. 5) are shown. The SA solution is shown by solid line in all plates. Top row: $j_{\max} = 40$, $P = 100$, dotted, dash-dotted and dashed lines correspond to time steps $\Delta t = 24$, 12 and 1 h, respectively. Second row: $P = 100$, $\Delta t = 1$ h, dotted, dash-dotted and dashed lines correspond to truncation degrees $j_{\max} = 10$, 20 and 40, respectively. Third row: $j_{\max} = 40$, $\Delta t = 1$ h, dotted, dash-dotted and dashed lines correspond to $P = 20$, 50 and 100 finite elements, respectively. Bottom row: solid and dashed lines are the same as above; dash-dotted lines show the solution by the SFE method.

Only the observable field at the surface ∂G is taken into account and the error is normalized by the time-averaged norm of the SA solution. For the high-resolution model, the initial large relative error as a result of the zero initial state is reduced below 2 per cent after $t = T_a$, and goes well below 1 per cent approximately $t = 2T_a$ after the onset of the time integration. Then the relative error oscillates with the frequency of the source but does not increase in long-term run. Naturally, for runs with lower spatial resolution or longer time step, the error is larger. The right plate in Fig. 7 shows a measure of divergence of **B** defined as ratio of norms

$$D(t) = \frac{||\mathrm{div}\,\mathbf{B}(t)||_{L_2}}{\langle ||\mathbf{B}||_{L_2} \rangle}. \tag{114}$$

We can see that after the initial increase following the switch-on, the magnetic monopoles do not accumulate and enforcing the solenoidality of **B** by additional constraints in the formulation is not necessary.

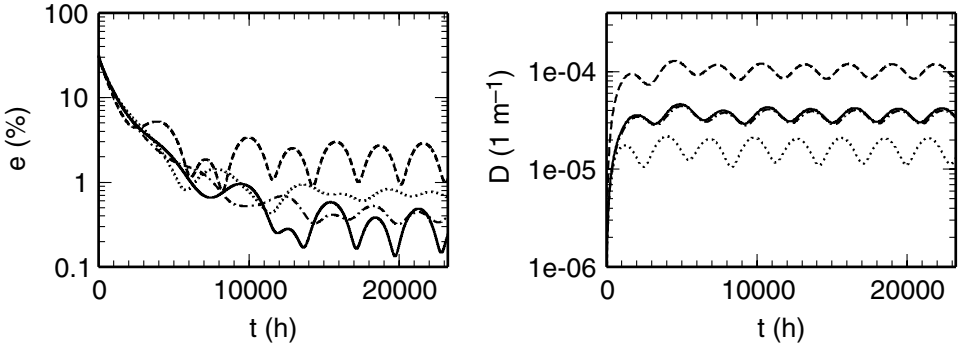

Figure 7. Left plate: relative error of the time-domain spherical harmonic-finite element (TD) solution with respect to the semi-analytical (SA) for model A, load 1a. Right plate: deviation from the divergence-free condition introduced by numerical errors during the time integration measured by the ratio $D(t)$ defined in eq. (114). The solid, dashed, dash-dotted and dotted lines correspond to solutions shown in Fig. 6 with discretization parameters ($j_{\max}$, P, Δt) set to (40, 100, 1 h), (40, 20, 1 h), (40, 100, 24 h) and (10, 100, 1 h), respectively.

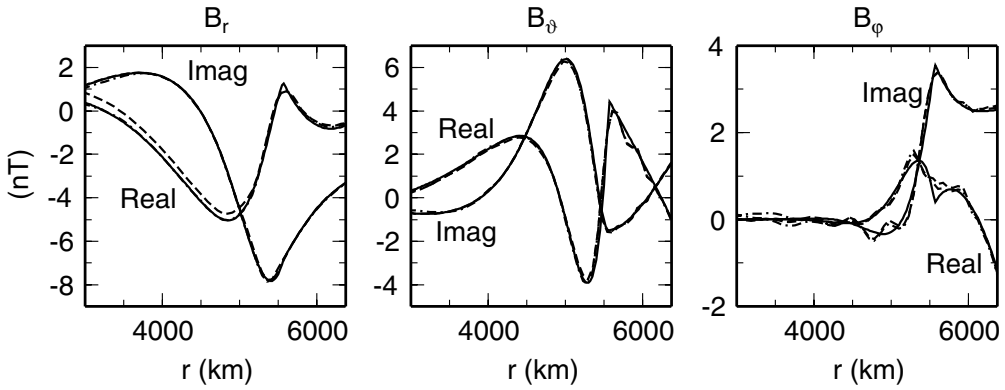

Figure 8. Comparison of the time-domain spherical harmonic-finite element (TD) method (dashed line) with the semi-analytical (SA) solution (solid line) for the conductivity model A excited by load 1b. Resolution of the TD method is set to ($j_{\max}$, P, Δt) = (40, 100, 1 h), the SA solution is truncated at $j_{\max}$ = 18. The SFE solution is also plotted by dash-dotted lines. The components of anomalous **B** are plotted along radius at fixed colatitude $\vartheta = 13^\circ$ and longitude $\varphi = 0^\circ$.

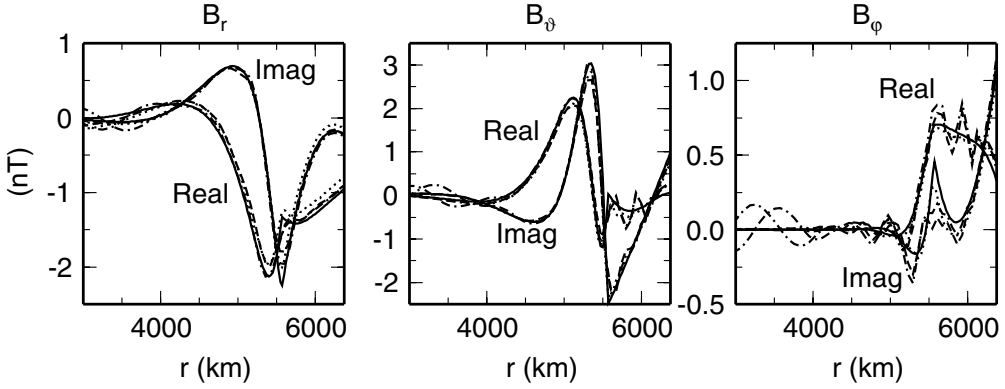

Figure 9. Comparison of the time-domain spherical harmonic-finite element (TD) method with the semi-analytical (SA) solution (solid line) for the conductivity model A excited by load 1c. Dashed and dotted lines correspond to resolutions ($j_{\max}$, P, Δt) = (40, 100, 1 h), and (80, 150, 0.1 h), respectively. The SA solution is truncated at $j_{\max}$ = 17. The SFE solution is also plotted by dash-dotted lines. The components of anomalous **B** are plotted along radius at fixed colatitude $\vartheta = 13^\circ$ and longitude $\varphi = 0^\circ$.

Figs 8 and 9 respectively show the results for model A excited by loads 1b and 1c at higher frequencies. In the case of load 1b, the accuracy of the TD method is $e(t) < 1$ per cent for $t \geq 3\ T_b$ (not shown). However, with the later load 1c corresponding to the period of 9 d and highly conductive model A, the amplitudes of anomalous field decrease and numerical errors in the form of oscillations with respect to radius in the upper 1000 km of the model become more visible. Because the same effect occurs in the frequency-domain SFE code, which uses the same spatial parametrization, these errors can be assigned to the inaccuracies in the spatial discretization, rather than to the time-integration scheme. Note that the discretization of conductivity given by eq. (80) implies that the surface of the spherical inclusion is actually rugged in the model approximation. The error evaluated on the surface is $e(t) < 2$ per cent for $t \geq 3T_c$. By increasing the resolution to ($j_{\max}$, P,

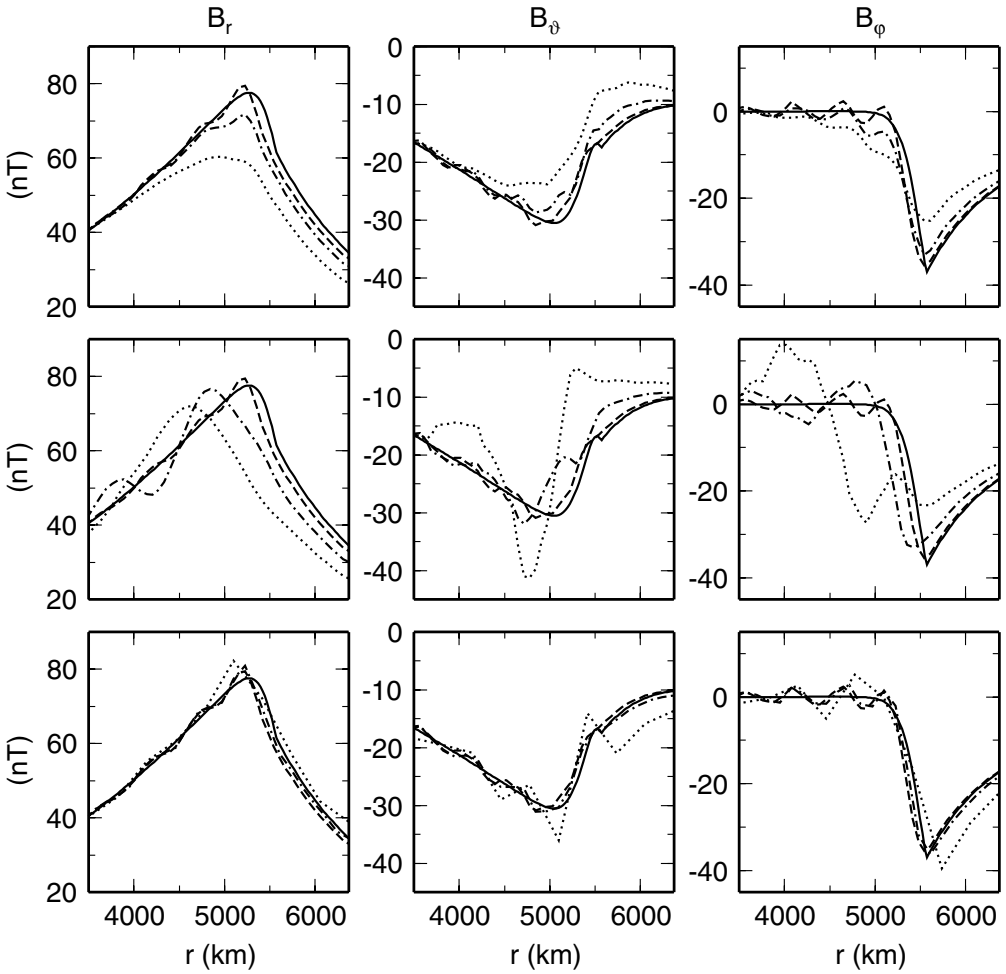

Figure 10. Resolution-dependent convergence of the time-domain spherical harmonic-finite element (TD) method towards the semi-analytical (SA) solution for the conductivity model B excited by load 2. The components of anomalous **B** with respect to the homogeneous sphere solution are plotted at $t = 96$ h. Colatitude and longitude are fixed at $\vartheta = 13^\circ$ and $\varphi = 0^\circ$. The SA solution is shown by a solid line in all plates. Top row: $j_{\max} = 40$, $P = 100$, dotted, dash-dotted and dashed lines correspond to time steps $\Delta t = 4$, 1 and 0.01 h, respectively. Middle row: $P = 100$, $\Delta t = 0.01$ h, dotted, dash-dotted and dashed lines correspond to truncation degrees $j_{\max} = 10$, 20 and 40, respectively. Bottom row: $j_{\max} = 40$, $\Delta t = 0.01$ h, dotted, dash-dotted and dashed lines correspond to $P = 20$, 50 and 100 finite elements, respectively.

$\Delta t) = (80, 150, 0.1$ h), further emphasized by using irregular radial grid (10-km stepping in the uppermost 500 km) the oscillatory behaviour can be suppressed and the error reduced below 1 per cent at a high computational cost.

Also the accuracy of the SA solution for this configuration is questionable. It breaks numerically when truncated at $j_{\max} \geq 18$ and stable solutions for $j_{\max} = 15 \ldots 17$ still differ considerably. The SA solution at $j_{\max} = 17$ is in best agreement with the TD and SFE solutions. It is obvious that no matter what technique we use, we are at the edge of numerical solvability of the problem and, for tests using higher-frequency or broad-spectrum transient signals, we have to switch to the more resistive models B and C.

Our next set of tests is performed in the time domain, using the transient load 2 excitation on models B and C. The reference SA solution is found for discretely sampled frequencies in the range 10^{-9}–10^{-4} rad s^{-1} (see Fig. 4). The spherical harmonic expansion is truncated at $j_{\max} = 18$ for frequencies below 5×10^{-6} rad s^{-1} and at $j_{\max} = 12$ for higher frequencies. The time evolution of $\mathbf{B}_{\mathrm{SA}}$ is computed by numerical evaluation of Fourier integrals of the frequency-domain solution.

Figs 10 and 11 respectively show the radial and time dependence of the TD and SA solutions for model B. As previously, only the anomalous field with respect to the homogenous sphere solution is shown. Results obtained by integration with long time steps show considerable delay behind the SA solution. This is a consequence of the explicit treating of the effect of lateral conductivity variations. Although the nested-spheres model B has the same geometry as the previous model A, increased conductivity contrast transfers more energy into the higher degree terms of the spherical harmonic series and good accuracy is obtained only for the highest truncation degree. Similarly to the previous case, small-scale radial oscillations can be seen in B_ϑ and B_φ, especially at larger depths where the amplitude of the field is small. In analogy with the previously discussed high-frequency tests, these oscillations are the result of the spatial Gibbs phenomenon caused by a large and sharp conductivity contrast. They can be suppressed by further increasing the spatial resolution.

Finally, Figs 12 and 13 compare the results for models B and C. Lower conductivity contrast in model C yields increased accuracy compared with model B at the same spatiotemporal resolution and the Gibbs phenomenon is prevented. Also note in Fig. 12 that the

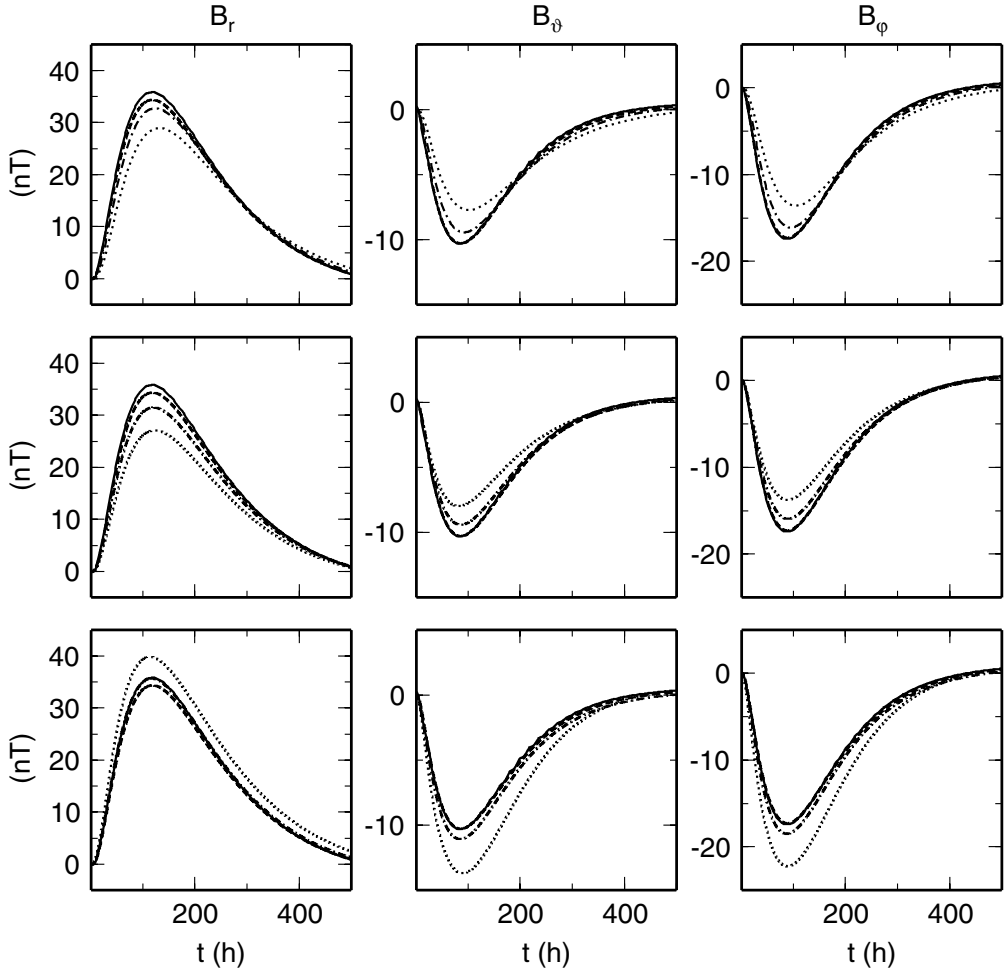

Figure 11. The same results as in Fig. 10. The time evolution of anomalous **B** is plotted at fixed colatitude $\vartheta = 13^\circ$ and longitude $\varphi = 0^\circ$, on the surface of the sphere.

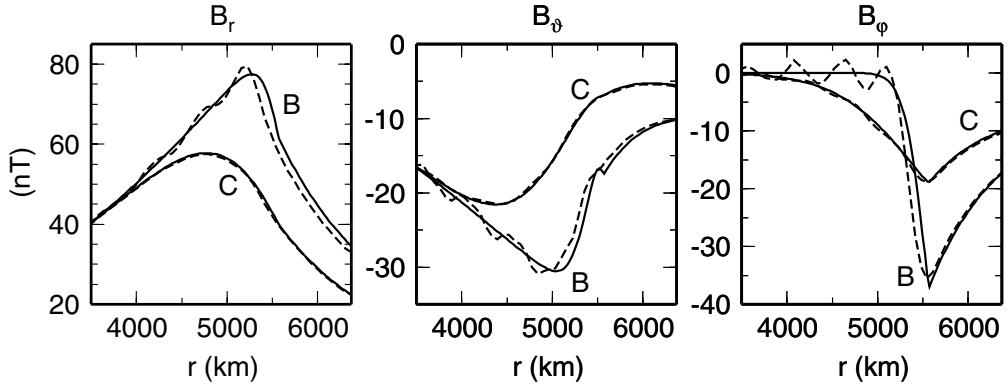

Figure 12. The components of anomalous **B** plotted along radius at $\vartheta = 13^\circ$, $\varphi = 0^\circ$ and $t = 96$ h. Nested-spheres models B and C are excited by load 2. The time-domain spherical harmonic-finite element (TD) solutions at ($j_{\max}$, P, Δt) = (40, 100, 0.01 h) discretization and the semi-analytical (SA) solutions are respectively shown by dashed and solid lines.

differences between the solutions for models B and C decrease close to the surface of the sphere. Despite this, at the peak of the storm, the results for the two models differ by 15 and 5 nT respectively in the vertical and horizontal components.

4 CONCLUSIONS

The TD approach to the problem of EM induction in the mantle of the heterogeneous Earth represents an alternative method to the traditional frequency-domain techniques. It is capable of computing the response of 3-D conductivity models to external excitation with complicated

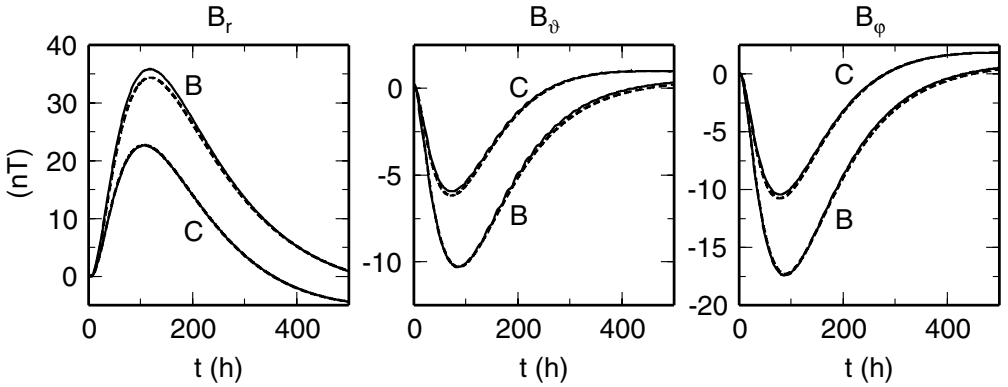

Figure 13. Same as Fig. 12 but **B** is plotted as a function of time at fixed colatitude $\vartheta = 13^\circ$ and longitude $\varphi = 0^\circ$, on the surface of the sphere.

spatiotemporal characteristics. The method has been numerically validated against SA solutions for nested-spheres conductivity models excited by harmonic variations of ring current, as well as by a simplified model of geomagnetic storm. Using eqs (13)–(15), the magnetic field computed at the surface of the Earth can be easily continued upwards to be compared with data recorded by satellite-born magnetometers. Implicit treatment of the effect of 1-D spherically symmetric conductivity stabilizes the time-integration scheme, while the computationally demanding coupling as a result of the lateral conductivity variations is efficiently evaluated on the angular grid using the solution from the previous time step. The spherical harmonic-finite element spatial parametrization allows one to increase the radial resolution where necessary, e.g. in the lithosphere, or throughout the transition zone in the mantle. On the other hand, the angular resolution given by the truncation degree of the spherical harmonic expansion can be increased only globally. Sharp lateral jumps in conductivity can lead to a spatial Gibbs phenomenon requiring very high spatial resolution for accurate results. In realistic conductivity models, this issue is of relatively small importance in the mantle. However, highly heterogeneous surface conductance reflecting the contrast between resistive continental rocks, conductive oceans and intermediate sediments (Everett *et al.* 2003) will require high spatial resolution and/or smoothing of discrete conductivity models. The time step has to be chosen cautiously with respect to the vigour of the time variations of the inducing magnetospheric currents.

The presented method is designed to be used as a forward solver in the global inversion of the satellite, or combined satellite and ground based data in the time domain, to reveal the lateral conductivity heterogeneities in the middle mantle. As a preliminary step, it was applied to compute the satellite altitude response of a realistic mantle conductivity model to a Dst transient signal (Velímský *et al.* 2003). The results suggest that the signal resulting from the mid-mantle lateral conductivity variations induced by intense geomagnetic storms should be detectable at satellite altitudes.

ACKNOWLEDGMENTS

The research presented in this paper was supported by grants nos 205/00/1367 and 205/03/1001 of the Grant Agency of the Czech Republic and by Charles University grant no. 238/2001/B-GEO/MFF. All figures were prepared using XFIG and GMT.

REFERENCES

Anderson, E. *et al.,* 1999. *LAPACK User's Guide,* 3rd edn, SIAM, Philadelphia.

Banks, R.J., 1969. Geomagnetic variations and the electrical conductivity of the upper mantle, *Geophys. J. R. astr. Soc.,* **17,** 457–487.

Daglis, I.A. & Kozyra, J.U., 2002. Outstanding issues of ring current dynamics, *J. Atmos. Solar Terr. Phys.,* **64,** 253–264.

Duffy, T.S. & Hemley, R.J., 1995. Some like it hot: The temperature structure of the Earth, *Rev. Geophys.,* **33,** Suppl., part 1, 5–10.

Everett, M.E. & Martinec, Z., 2003. Spatiotemporal response of a conducting sphere under simulated geomagnetic storm conditions, *Phys. Earth planet. Int.,* **138,** 163–181.

Everett, M.E. & Schultz, A., 1995. Geomagnetic induction in eccentrically nested spheres, *Phys. Earth planet. Int.,* **92,** 189–198.

Everett, M.E. & Schultz, A., 1996. Geomagnetic induction in a heterogeneous sphere: Azimuthally symmetric test computations and the response of an undulating 660-km discontinuity, *J. geophys. Res.,* **101**(B2), 2765–2783.

Everett, M.E., Constable, S. & Constable, C., 2003. Effects of near-surface conductance on global satellite induction responses, *Geophys. J. Int.,* **153,** 277–286.

Fainberg, E.B., Kuvshinov, A.V. & Singer, B.Sh., 1990. Electromagnetic induction in a spherical earth with non-uniform oceans and continents in electric contact with the underlying medium—I. Theory, method and example, *Geophys. J. Int.,* **102,** 273–281.

Hamano, Y., 2002. A new time-domain approach for the electromagnetic induction problem in a three-dimensional heterogeneous earth, *Geophys. J. Int.,* **150,** 753–769.

Křížek, M. & P. Neittaanmäki, 1990. *Finite Element Approximation of Variational Problems and Applications,* Longman Scientific and Technical, Harlow, and Wiley, New York.

Kuvshinov, A.V. & Pankratov, O.V., 1994. Electromagnetic induction in a spherical Earth with inhomogeneous conducting mantle: thin sheet forward problem. In: *Proc. 12th workshop on electromagnetic induction in the Earth,* p. 53, ed. Menvielle, M., Université de Bretagne Occidentale, Brest, France.

Langel, R.A., 1987. The main field, in, *Geomagnetism,* Vol. 1, pp. 249–512, ed. Jacobs J.A., Academic Press, London.

Martinec, Z., 1989. Program to calculate the spectral harmonic expansion coefficients of the two scalar fields product, *Comput. Phys. Commun.,* **54,** 177–182.

Martinec, Z., 1997. Spectral-finite element approach to two-dimensional electromagnetic induction in a spherical Earth, *Geophys. J. Int.,* **130,** 583–594.

Martinec, Z., 1998. Geomagnetic induction in multiple eccentrically nested spheres, *Geophys. J. Int.,* **132,** 96–110.

Martinec, Z., 1999. Spectral-finite element approach to three-dimensional electromagnetic induction in a spherical Earth, *Geophys. J. Int.,* **136,** 229–250.

Martinec, Z., Everett, M.E. & Velímský, J., 2003. Time-domain, spectral-finite element approach to transient two-dimensional geomagnetic induction in a spherical heterogoeneous earth, *Geophys. J. Int.,* **155,** 33–43.

Parkinson, W.D. & Hutton, V.R.S., 1989. The electrical conductivity of the Earth, in, *Geomagnetism,* Vol. 3, pp. 261–321, ed. Jacobs J.A., Academic Press, London.

Press, W.H., Teukolsky, S.A., Vetterling, W.T. & Flannery, B.P., 1992. *Numerical recipes in Fortran. The art of scientific computing,* Cambridge University Press, Cambridge.

Schultz, A. & Larsen, J., 1987. On the electrical conductivity of the mid mantle: I. Calculation of equivalent scalar magnetotelluric response functions, *Geophys. J. R. astr. Soc.,* **88,** 733–761.

Tarits, P., 1994. Electromagnetic studies of global geodynamic processes, *Surv. Geophys.,* **15,** 209–238.

Uyeshima, M. & Schultz, A., 2000. Geoelectromagnetic induction in a heterogeneous sphere: a new three-dimensional forward solver using a conservative staggered-grid finite difference method, *Geophys. J. Int.,* **140,** 636–650.

Varshalovich, D.A., Moskalev, A.N. & Khersonskii, V.K., 1989. *Quantum Theory of Angular Momentum,* World Scientific, Singapore.

Velímský, J., Everett, M.E. & Marinec, Z., 2003. The transient Dst electromagnetic induction signal at satellite altitudes for a realistic 3-D electrical conductivity in the crust and mantle, *Geophys. Res. Lett.,* **30**(7), 1355–1359.

Xu, Y., Poe, B.T., Shankland, T.J. & Rubie, D.C., 1998. Electrical conductivity of olivine, wadsleyite, and ringwoodite under upper-mantle conditions, *Science,* **280,** 1415–1418.

Yoshimura, R. & Oshiman, N., 2002. Edge-based finite element approach to the simulation of geolectromagnetic induction in a 3-D sphere, *Geophys. Res. Lett.,* **29**(3), 1039–1043.

Zhang, T.S. & Schultz, A., 1992. A 3-D perturbation solution for the EM induction problem in a spherical earth—the forward problem, *Geophys. J. Int.,* **111,** 319–334.

APPENDIX A: SPHERICAL HARMONIC FUNCTIONS

We expand scalar functions into series of fully normalized scalar spherical harmonic functions Y_{jm} (Varshalovich *et al.* 1989, p. 130),

$$Y_{jm}(\Omega) = \sqrt{\frac{2j+1}{4\pi}\frac{(j-m)!}{(j+m)!}}\,P_j^m(\cos\vartheta)e^{im\varphi} = P_{jm}(\cos\vartheta)e^{im\varphi}, \tag{A1}$$

where $P_{jm}(\cos\vartheta)$ is the normalized form of associated Legendre polynomials $P_j^m(\cos\vartheta)$. The spherical harmonic functions are orthonormal on a unit sphere,

$$\int_\Omega \overline{Y}_{jm}(\Omega)\cdot Y_{j'm'}(\Omega)\,\mathrm{d}\Omega = \delta_{jj'}\delta_{mm'},$$

and are eigenfunctions of the angular part of the the Laplace operator,

$$\left[\frac{1}{\sin\vartheta}\frac{\partial}{\partial\vartheta}\left(\sin\vartheta\frac{\partial}{\partial\vartheta}\right)+\frac{1}{\sin^2\vartheta}\frac{\partial^2}{\partial\varphi^2}\right]Y_{jm}(\Omega) = -j(j+1)Y_{jm}(\Omega). \tag{A2}$$

Similarly, vector functions can be expanded into series of vector spherical harmonics. From several different sets of orthogonal vector spherical harmonic functions suggested by Varshalovich *et al.* (1989, p. 208), we prefer the following one:

$$\left\{\mathbf{S}_{jm}^{(\lambda)}(\Omega)\,|\,j=0,\ldots,\infty, m=-j,\ldots,j, \lambda=-1,0,1\right\}, \tag{A3}$$

where

$$\mathbf{S}_{jm}^{(0)}(\Omega) = \mathbf{e}_r\times\mathrm{grad}_\Omega Y_{jm}(\Omega) = \left[\frac{\partial Y_{jm}(\Omega)}{\partial\vartheta}\mathbf{e}_\varphi - \frac{1}{\sin\vartheta}\frac{\partial Y_{jm}(\Omega)}{\partial\varphi}\mathbf{e}_\vartheta\right], \tag{A4}$$

$$\mathbf{S}_{jm}^{(-1)}(\Omega) = Y_{jm}(\Omega)\mathbf{e}_r, \tag{A5}$$

$$\mathbf{S}_{jm}^{(1)}(\Omega) = \mathrm{grad}_\Omega Y_{jm}(\Omega) = \left[\frac{\partial Y_{jm}(\Omega)}{\partial\vartheta}\mathbf{e}_\vartheta + \frac{1}{\sin\vartheta}\frac{\partial Y_{jm}(\Omega)}{\partial\varphi}\mathbf{e}_\varphi\right]. \tag{A6}$$

The angular part of the gradient operator is

$$\mathrm{grad}_\Omega = \mathbf{e}_\vartheta\frac{\partial}{\partial\vartheta} + \mathbf{e}_\varphi\frac{1}{\sin\vartheta}\frac{\partial}{\partial\varphi}, \tag{A7}$$

and $\mathbf{e}_r$, $\mathbf{e}_\vartheta$ and $\mathbf{e}_\varphi$ denote unit vectors corresponding to the radial coordinate r, colatitude ϑ and longitude φ, respectively. Functions $\mathbf{S}_{jm}^{(0)}(\Omega)$ are toroidal; functions $\mathbf{S}_{jm}^{(-1)}(\Omega)$ and $\mathbf{S}_{jm}^{(1)}(\Omega)$ represent the radial and angular component of the spheroidal part of the expanded field, respectively. Although $\mathbf{S}_{jm}^{(\lambda)}(\Omega)$ are not eigenfunction of the Laplace operator, separation of the radial component generally simplifies the evaluation of coupling in problems with laterally varying parameters. Functions $\mathbf{S}_{jm}^{(\lambda)}(\Omega)$ are orthogonal on a unit sphere, i.e.

$$\int_\Omega \overline{\mathbf{S}}_{jm}^{(\lambda)}(\Omega)\cdot\mathbf{S}_{j'm'}^{(\lambda')}(\Omega)\,\mathrm{d}\Omega = N_{j\lambda}\delta_{jj'}\delta_{mm'}\delta_{\lambda\lambda'}, \tag{A8}$$

with the norm

$$N_{j\lambda} = (1-\delta_{-1\lambda})\Pi_j + \delta_{-1\lambda}, \tag{A9}$$

$$\Pi_j = j(j+1). \tag{A10}$$

Because the Maxwell equations do not admit the existence of magnetic monopoles, the zeroth order spherical harmonic functions $Y_{00}(\Omega)$ and $\mathbf{S}^{(\lambda)}{}_{00}(\Omega)$ are excluded from the parametrizations of the scalar magnetic potential (10)–(12) and magnetic induction vector (19), respectively.

From definitions (A4)–(A6), the following relations can be easily derived:

$$\mathbf{S}^{(\lambda)}_{j-m}(\Omega) = (-1)^m \overline{\mathbf{S}}^{(\lambda)}_{jm}(\Omega), \tag{A11}$$

$$\mathbf{e}_r \times \mathbf{S}^{(0)}_{jm}(\Omega) = -\mathbf{S}^{(1)}_{jm}(\Omega), \tag{A12}$$

$$\mathbf{e}_r \times \mathbf{S}^{(-1)}_{jm}(\Omega) = 0, \tag{A13}$$

$$\mathbf{e}_r \times \mathbf{S}^{(1)}_{jm}(\Omega) = \mathbf{S}^{(0)}_{jm}(\Omega), \tag{A14}$$

$$\operatorname{grad}\left[f(r)Y_{jm}(\Omega)\right] = \frac{df(r)}{dr}\mathbf{S}^{(-1)}_{jm}(\Omega) + \frac{f(r)}{r}\mathbf{S}^{(1)}_{jm}(\Omega), \tag{A15}$$

$$\operatorname{curl}\left[f(r)\mathbf{S}^{(0)}_{jm}(\Omega)\right] = -\Pi_j \frac{f(r)}{r}\mathbf{S}^{(-1)}_{jm}(\Omega) - \left(\frac{d}{dr} + \frac{1}{r}\right) f(r)\mathbf{S}^{(1)}_{jm}(\Omega), \tag{A16}$$

$$\operatorname{curl}\left[f(r)\mathbf{S}^{(-1)}_{jm}(\Omega)\right] = -\frac{f(r)}{r}\mathbf{S}^{(0)}_{jm}(\Omega), \tag{A17}$$

$$\operatorname{curl}\left[f(r)\mathbf{S}^{(1)}_{jm}(\Omega)\right] = \left(\frac{d}{dr} + \frac{1}{r}\right) f(r)\mathbf{S}^{(0)}_{jm}(\Omega), \tag{A18}$$

$$\operatorname{div}\left[f(r)\mathbf{S}^{(0)}_{jm}(\Omega)\right] = 0, \tag{A19}$$

$$\operatorname{div}\left[f(r)\mathbf{S}^{(-1)}_{jm}(\Omega)\right] = \left(\frac{d}{dr} + \frac{2}{r}\right) f(r)Y_{jm}(\Omega), \tag{A20}$$

$$\operatorname{div}\left[f(r)\mathbf{S}^{(1)}_{jm}(\Omega)\right] = -\Pi_j \frac{f(r)}{r}Y_{jm}(\Omega). \tag{A21}$$

By $f(r)$ we mean an arbitrary continuous function of radius r.

APPENDIX B: OVERVIEW OF FUNCTIONAL SPACES

$C(G)^k$ space of scalar ($k = 1$) and vector ($k = 3$) functions continuous on the domain G

$C^n(G)^k$ space of scalar ($k = 1$) and vector ($k = 3$) functions whose classical derivatives up to the nth order belong to $C(G)^k$

$C^1(\langle 0,\infty\rangle)^k$ space of scalar ($k = 1$) and vector ($k = 3$) functions continuously differentiable with respect to t on interval $\langle 0, \infty)$

$D^0(G)$ space of smooth (infinitely differentiable) scalar functions with compact support in G, which are zero on ∂G

$L_2(G)^k$ space of scalar ($k = 1$), vector ($k = 3$) and tensor ($k = 9$) functions that are square integrable in G; the scalar products

$$(f, g) = \int_G fg \, \mathrm{d}V,$$

$$(\mathbf{f}, \mathbf{g}) = \int_G \mathbf{f}\cdot\mathbf{g} \, \mathrm{d}V,$$

of functions from $L_2(G)^1$ and $L_2(G)^3$, respectively, induce the norms

$$||f||_{L_2} = (f, f)^{\frac{1}{2}},$$

$$||\mathbf{f}||_{L_2} = (\mathbf{f}, \mathbf{f})^{\frac{1}{2}}$$

$L_\infty{}^+(G)$ space of positive ($f > 0$) scalar functions bounded in G; the norm in $L^+_\infty(G)$ is defined as

$$||f||_{L_\infty} = \max_G |f| \tag{B3}$$

$W^{1,2}(G)^k$ Sobolev's space of scalar ($k = 1$) and vector ($k = 3$) functions from $L_2(G)^k$ whose partial derivatives belong to $L_2(G)^{3k}$; the scalar products

$$(f, g)_{W^{1,2}} = \int_G [fg + \operatorname{grad} f \cdot \operatorname{grad} g] \, \mathrm{d}V,$$

$$(\mathbf{f}, \mathbf{g})_{W^{1,2}} = \int_G \left[\mathbf{f}\cdot\mathbf{g} + \operatorname{grad}\mathbf{f} : (\operatorname{grad}\mathbf{g})^T\right] \mathrm{d}V,$$

of functions from $W^{1,2}(G)^1$ and $W^{1,2}(G)^3$, respectively, induce the norms

$$||f||_{W^{1,2}} = (f, f)^{\frac{1}{2}}_{W^{1,2}},$$

$$||\mathbf{f}||_{W^{1,2}} = (\mathbf{f}, \mathbf{f})^{\frac{1}{2}}_{W^{1,2}}$$

H_{curl} space of vector functions from $L_2(G)^3$ whose rotation also belongs to $L_2(G)^3$; the scalar product

$$(\mathbf{f}, \mathbf{g})_{H_{\mathrm{curl}}} = \int_G [\mathbf{f} \cdot \mathbf{g} + \mathrm{curl}\,\mathbf{f} \cdot \mathrm{curl}\,\mathbf{g}]\ \mathrm{d}V,$$

induces the norm

$$|\mathbf{f}||_{H_{\mathrm{curl}}} = (\mathbf{f}, \mathbf{f})^{\frac{1}{2}}_{H_{\mathrm{curl}}}$$

$H_{\mathrm{curl},0}$ space of vector functions from H_{curl} whose tangential component is zero on the boundary ∂G